https://doi.org/10.5194/egusphere-2026-3107
Preprint. Discussion started: 15 June 2026

Beyond hydraulic diffusion: reaction front propagation and timescales in metamorphic (de)volatilization processes

Liudmila Khakimova[1], Stefan M. Schmalholz[1], and Yury Y. Podladchikov[1]
[1]Institute of Earth Sciences, University of Lausanne, 1015 Lausanne, Switzerland
Correspondence: Liudmila Khakimova (liudmila.khakimova@unil.ch)

Abstract. Metamorphic (de)volatilization reactions play fundamental roles in many geodynamic processes and are frequently associated with propagating reaction fronts, yet the mechanisms controlling front propagation remain poorly constrained. Here, we derive new analytical solutions for fluid pressure-driven (de)volatilization reaction fronts in porous rocks. The solutions predict that reaction-zone width increases with the square root of time, a scaling that arises from mass conservation across the moving reaction front rather than from classical hydraulic pore-pressure diffusion. Front propagation is governed by an effective diffusivity that depends on both hydraulic and chemical parameters, including reaction-induced density changes. Unlike conventional hydraulic diffusivity, which neglects reaction-induced density variations and generally predicts much faster propagation, the effective diffusivity captures the retardation of reaction fronts caused by density changes, with larger reaction-induced density changes producing slower propagation. In addition to a single-front formulation, we derive an analytical solution for two simultaneously propagating, coupled reaction fronts. The fronts are dynamically linked through mass conservation, preventing independent propagation and causing the leading front to advance faster than the trailing front. Both the single- and two-front solutions closely match numerical simulations. Application of the two-front model to published gypsum dehydration experiments shows that accounting for pore-water to pore-vapor transitions yields more realistic permeability estimates than single-front models. Application to natural metamorphic reactions predicts permeabilities between 10^{-18} and 10^{-24} m^2, consistent with independent experimental, geophysical, and geological estimates. By analogy, the analytical framework can also be extended to chemically controlled reaction fronts governed solely by chemical diffusion. The analytical solutions provide a quantitative framework for estimating the timescales of natural and experimental (de)volatilization processes involving propagating reaction fronts.

1 Introduction

Mineral reactions involving (de)volatilization and phase transitions are governed by variations in pressure, temperature, or chemical composition (e.g., Philpotts and Ague, 2022). These processes play a central role in a wide range of geodynamic processes, such as the water cycle at subduction zones (e.g., Schmidt and Poli, 1998; Bebout, 2014; Vitale Brovarone et al., 2020), serpentinisation and eclogitisation (e.g., Austrheim, 1987; Schrenk et al., 2013; Pettke and Bretscher, 2022), or dehydration-induced seismicity (e.g., Raleigh and Paterson, 1965; Brantut et al., 2012; Okazaki and Hirth, 2016; Porkoláb et al., 2025; Markmann and Lanari, 2026), as well as in geological applications, including the storage of carbon dioxide in geological

https://doi.org/10.5194/egusphere-2026-3107
Preprint. Discussion started: 15 June 2026

reservoirs by mineral carbonation (Matter and Kelemen, 2009). Here, we use the term reaction in a broad sense to refer to volatilization (e.g., hydration), devolatilization (e.g., dehydration), and phase transitions, including, for example, the transition of pore water into pore vapor. The temporal and spatial progression of reactions is frequently associated to the propagation of a reaction front, for example during mineral replacement reactions (e.g., Putnis, 2009), the hydration of granulite to form eclogite (e.g., Austrheim, 1987; Kaatz et al., 2023), the dehydration of serpentinite (e.g., Padrón-Navarta et al., 2011), the alteration of serpentinite by influx of carbon-bearing aqueous fluid (e.g., Beinlich et al., 2020), the serpentinization of peridotite (e.g., Debret et al., 2013) or the dehydration of gypsum (e.g., Fusseis et al., 2012). In the context of more applied systems, reaction fronts occur during the leaching of cement (e.g., Mainguy and Coussy, 2000) or the sequestration of carbon dioxide by concrete carbonation (e.g., Papadakis et al., 1991a, b; Galan et al., 2010).

Laboratory experiments, analytical solutions and numerical simulations consistently demonstrate that the position of many reaction fronts scales with the square root of time (e.g., Aiki and Muntean, 2013; Papadakis et al., 1991a; Fusseis et al., 2012; Mainguy and Coussy, 2000; Schmalholz et al., 2024; Stefan, 1891). The classical solution for the propagation of a reaction front scaling with the square root of time was derived by Stefan (1891) to describe the temperature-controlled phase transition from water to ice and to predict the moving ice-water boundary during freezing of a water column, the so-called Stefan problem (e.g., Gupta, 2017). Stefan-like solutions can be directly applied to geodynamic melting-solidification processes, for example the solidification of a magma lake (e.g., Turcotte and Schubert, 2014). Stefan-like solutions have also been applied to describe chemically controlled reaction fronts associated with calcium leaching and chloride penetration in concrete (e.g., Mainguy and Coussy, 2000; Coussy, 2004). Alternatively, for chemically-controlled reactions the square root of time scaling was derived analytically based on a mass balance approach for reaction front propagation during concrete carbonation (e.g., Papadakis et al., 1991b).

The propagation of (de)volatilization fronts is commonly associated with porous fluid flow driven by fluid pressure gradients different from the hydrostatic gradient (e.g., Connolly, 1997; Sulem and Famin, 2009; Poulet et al., 2014; Karrech et al., 2018; Bras et al., 2023; Huber et al., 2022; Schmalholz et al., 2024). Laboratory experiments, theoretical models and molecular dynamics simulations show that the fluid pressure controls not only porous flow, but can also control the reaction itself since it governs the chemical potential of the fluid phase (e.g., Dahlen, 1992; Llana-Fúnez et al., 2012; Mazzucchelli et al., 2024, 2026). Hence, for reactions involving a fluid phase, variations in fluid pressure can trigger (de)volatilization reactions in the same way than variations in temperature or in chemical composition. A scaling of the reaction front position with the square root of time was also shown with numerical simulations for pressure-controlled reactions including the hydration of granulite (Bras et al., 2023) and the dehydration of serpentinite (Schmalholz et al., 2024), as well as with laboratory dehydration experiments of gypsum (Fusseis et al., 2012).

In the mathematical relation between reaction front position and square root of time, the time must be multiplied due to dimensional consistency with a term having units of a diffusivity, that is m^2/s. We refer to this diffusivity term as effective diffusivity. Many metamorphic (de)volatilization processes in nature are likely governed by the propagation of reaction fronts, and hence by an effective diffusivity. If this effective diffusivity would be known or could be calculated, then the time scales for the spatial progression of metamorphic (de)volatilization processes could be predicted. However, for pressure-controlled

https://doi.org/10.5194/egusphere-2026-3107
Preprint. Discussion started: 15 June 2026

(de)volatilization reactions no analytical solution and no explicit equation for the effective diffusivity has been derived yet. Because of this gap, the timescales of many metamorphic (de)volatilization processes cannot be predicted. These timescales are also important for reactions that do not directly involve fluids, because fluids can accelerate nominally fluid-absent reactions by several orders of magnitude (e.g., Liu et al., 2025). Metamorphic devolatilization is a major source of such fluids.

Here, we employ a hydro-chemical mathematical model to derive an analytical solution for the propagation of pressure-controlled (de)volatilization fronts that can involve a single reaction front or two coupled reaction fronts, for example, the dehydration of a rock and the transition of the liberated pore water to pore vapor. We show that the square root of time scaling results from the mass balance across the moving reaction front and not from hydraulic pore pressure diffusion. Furthermore, we compare the new analytical solution with previously published numerical solutions of Schmalholz et al. (2024) and with new numerical solutions. We also apply the solution to several (de)hydration reactions common in geodynamics to estimate effective diffusivities and timescales for natural (de)hydration zones. Moreover, we discuss the application of our analytical solution to published experimental gypsum dehydration results (e.g., Fusseis et al., 2012; Leclère et al., 2018).

2 Mathematical model for reaction front propagation

2.1 Analytical solution: single reaction front

The conservation equation of total mass in the absence of diffusive fluxes, for negligible solid velocities and in 1D is a partial differential equation (PDE) (e.g., Fowler, 1985):

$$\frac{\partial \rho_{\text{total}}}{\partial t} + \frac{\partial}{\partial x}\left[\rho_{\text{fluid}}\, q_D\right] = 0, \tag{1}$$

where t is time, x the spatial coordinate, the total rock density $\rho_{\text{total}} = \rho_{\text{fluid}}\,\varphi + \rho_{\text{solid}}\,(1-\varphi)$, with ρ_{fluid} and ρ_{solid} being fluid and solid densities, respectively, φ being porosity and q_D being the Darcy flux:

$$q_D = -\frac{k}{\eta}\frac{\partial P}{\partial x}, \tag{2}$$

where $k = k_0(\varphi/\varphi_0)^n$ with k_0 being a reference permeability, φ_0 a reference porosity, n an exponent, η the fluid viscosity, and P the fluid pressure. We introduce a moving-frame coordinate tied to the propagating reaction front using

$$z = x - x_{\text{front}}(t), \qquad \frac{d}{dt}x_{\text{front}}(t) = v_{\text{front}}(t), \tag{3}$$

where $x_{\text{front}}(t)$ and $v_{\text{front}}(t)$ are the instantaneous front position and velocity, respectively (Fig. 1). Under this change of variables, the derivatives transform as

$$\left.\frac{\partial}{\partial t}\right|_x = \left.\frac{\partial}{\partial t}\right|_z - v_{\text{front}}(t)\,\frac{\partial}{\partial z}, \quad \frac{\partial}{\partial x} = \frac{\partial}{\partial z}. \tag{4}$$

Substituting equation (4) into (1), assuming a steady-state moving frame (i.e. $\partial/\partial t|_z = 0$, representing a quasi-stationary approximation) and using total derivatives if the corresponding quantities only depend on a single variable yields an ordinary

https://doi.org/10.5194/egusphere-2026-3107
Preprint. Discussion started: 15 June 2026

differential equation (ODE) in z:

$$-v_{\text{front}}(t)\frac{d}{dz}\left[\rho_{\text{total}}(z)\right]+\frac{d}{dz}\left[\rho_{\text{fluid}}(z)q_D(z)\right]=0. \tag{5}$$

$v_{\text{front}}(t)$ depends only on time and is independent of the spatial coordinate z, since it represents the velocity of the entire moving reference frame. Therefore, $v_{\text{front}}(t)$ in equation (5) can be treated as constant with respect to z, and equation (5) can be transformed into:

$$\frac{d}{dz}\left[-v_{\text{front}}(t)\rho_{\text{total}}(z)+\rho_{\text{fluid}}(z)q_D(z)\right]=0. \tag{6}$$

Equation (6) implies that the term inside the derivative, d/dz, is constant in z and does not change across the reaction front. In the following, we distinguish quantities ahead and behind the reaction front, whereby ahead refers to the region the front has not yet reached and behind refers to the region the front has already passed through (Fig. 1). Evaluating terms immediately behind ($z = z_{\text{behind}}$) and ahead ($z = z_{\text{ahead}}$) of the reaction front provides a so-called jump condition across the front:

$$\left[v_{\text{front}}(t)\,\rho_{\text{total}}(z)+\rho_{\text{fluid}}(z)\,q_D(z)\right]\Big|_{z=z_{\text{behind}}}=\left[v_{\text{front}}(t)\,\rho_{\text{total}}(z)+\rho_{\text{fluid}}(z)\,q_D(z)\right]\Big|_{z=z_{\text{ahead}}}. \tag{7}$$

The only assumption for this jump condition is that the reaction front is sharp, which means its thickness is negligible compared to the characteristic length of the system.

In the region ahead of the front, we assume that the fluid and solid are in mechanical equilibrium, so that fluid pressure is spatially uniform and its gradient negligible (Fig. 1). Hence,

$$q_D(z_{\text{ahead}})\approx 0. \tag{8}$$

Within the region behind the reaction front, we assume that hydraulic diffusion is significantly faster than the motion of the front. Consequently, the fluid pressure reaches equilibrium almost instantaneously with respect to the front propagation. Under this approximation, the Darcy flux in the region behind the front is (Fig. 1):

$$q_D(z_{\text{behind}})\approx\varphi\, v_{\text{fluid}}\approx-\frac{k(z_{\text{behind}})}{\eta}\frac{\Delta P}{x_{\text{front}}(t)}, \tag{9}$$

where the pressure difference behind the reaction front is:

$$\Delta P=P(z_{\text{boundary}})-P(z_{\text{behind}}), \tag{10}$$

with $P(z_{\text{boundary}})$ being the fluid pressure at the boundary, and $P(z_{\text{behind}})$ being the pressure just behind the front (Fig. 1). Substituting equations (8) and (9) into (7) and rearranging provides

$$v_{\text{front}}\Delta\rho_{\text{total}}=\rho_{\text{fluid}}(z_{\text{behind}})\frac{k(z_{\text{behind}})}{\eta}\frac{\Delta P}{x_{\text{front}}(t)}, \tag{11}$$

with $\Delta\rho_{\text{total}}=\rho_{\text{total}}(z_{\text{behind}})-\rho_{\text{total}}(z_{\text{ahead}})$. We introduce an effective diffusivity D_{eff}:

$$D_{\text{eff}}=\frac{\rho_{\text{fluid}}(z_{\text{behind}})}{\Delta\rho_{\text{total}}}\frac{k(z_{\text{behind}})}{\eta}\Delta P. \tag{12}$$

https://doi.org/10.5194/egusphere-2026-3107
Preprint. Discussion started: 15 June 2026

Substituting equation (12) into (11) yields

$$v_{\mathrm{front}}(t) = \frac{D_{\mathrm{eff}}}{x_{\mathrm{front}}(t)}. \tag{13}$$

Using $v_{\mathrm{front}}(t) = dx_{\mathrm{front}}(t)/dt$, we obtain an ODE for the temporal evolution of the reaction front position:

$$\frac{dx_{\mathrm{front}}(t)}{dt} = \frac{D_{\mathrm{eff}}}{x_{\mathrm{front}}(t)}. \tag{14}$$

To solve this ODE, we separate the variables and integrate with the initial condition $x_{\mathrm{front}}(t=0) = 0$:

$$\int_0^{x_{\mathrm{front}}(t)} x_{\mathrm{front}}\, dx_{\mathrm{front}} = \int_0^{t} D_{\mathrm{eff}}\, dt. \tag{15}$$

The integration yields:

$$\frac{1}{2}\, x_{\mathrm{front}}^2(t) = D_{\mathrm{eff}}\, t. \tag{16}$$

Hence,

$$x_{\mathrm{front}}(t) = \sqrt{2\, D_{\mathrm{eff}}\, t}\,. \tag{17}$$

Notably, $x_{\mathrm{front}}(t)$ depends on the square root of time, although the process governing front propagation is not described by a diffusion-like PDE but by an ODE (equation 14).

2.2 Analytical solution: two coupled reaction fronts

We elaborate the analytical solution for the propagation of a single reaction front to two reaction fronts. The derivation is also based on the conservation equation for total mass, jump conditions at the two fronts and a quasi-stationary approximation. The detailed derivation is given in Appendix A. The time evolution of the positions of the two reaction fronts, x_1 (being the front ahead) and x_2 (being the front behind), is:

$$x_1(t) = \lambda_1 \sqrt{t}, \qquad x_2(t) = \lambda_2 \sqrt{t}, \tag{18}$$

with

$$\lambda_1 = \sqrt{\frac{2D_{\mathrm{eff},1}}{1-r}}, \qquad \lambda_2 = r\lambda_1. \tag{19}$$

The parameter r is derived in Appendix A and involves the two effective diffusivities $D_{\mathrm{eff},1}$ and $D_{\mathrm{eff},2}$ which are associated with reaction front 1 and 2, respectively. These diffusivities have the same expression as the diffusivity for a single reaction front, equation (12), with the values corresponding to the respective reaction front (see Appendix A). Equations (18) and (19) show that the two reaction fronts cannot propagate independently because they are coupled via the parameter r. The reason for this coupling is that the total mass within the region between the two reaction fronts must be conserved.

https://doi.org/10.5194/egusphere-2026-3107
Preprint. Discussion started: 15 June 2026

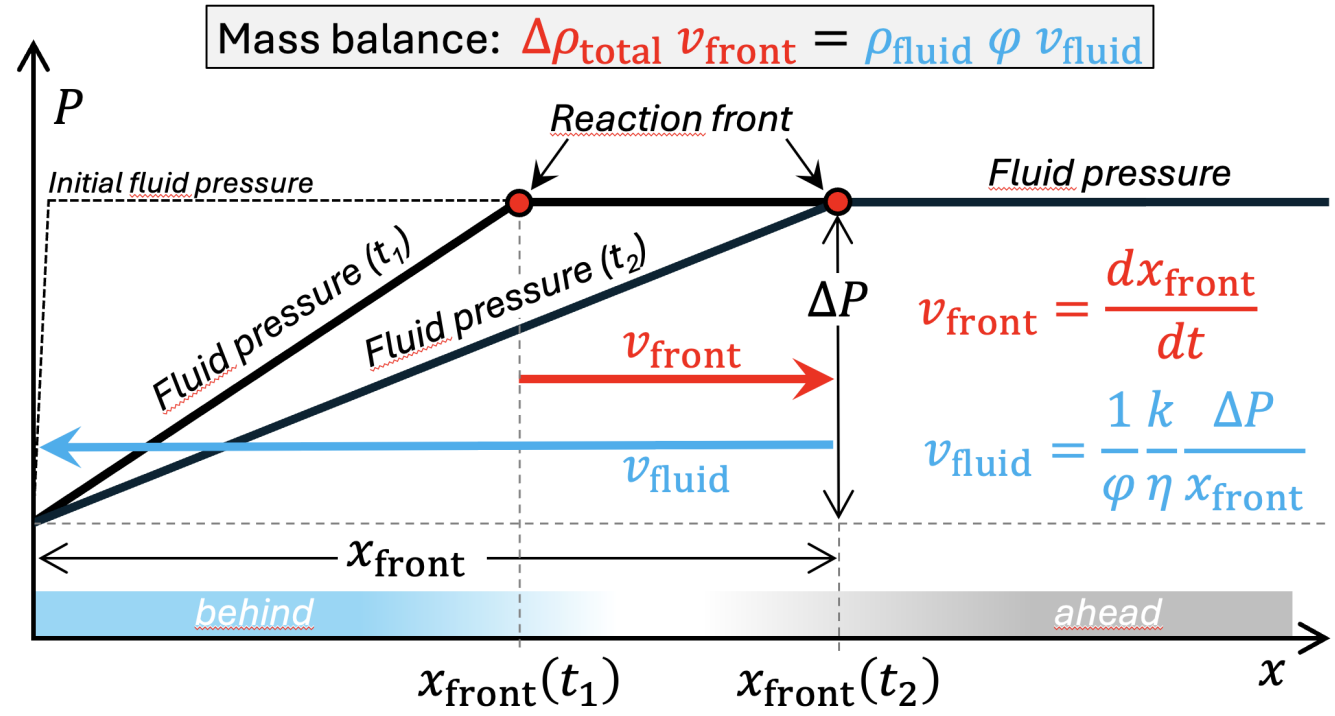

Figure 1. Sketch indicating the fluid pressure profile around a propagating dehydration reaction front, the propagation velocity of the reaction front, v_{front}, and the velocity of the pore fluid, v_{fluid}, liberated by the dehydration reaction (see text for derivation of the presented equations). The sketched evolution of the fluid pressure profile is very similar to the fluid pressure profiles in the performed numerical simulations and the black dashed line indicates the initial fluid pressure profile applied in the simulations (see Fig. 2b).

2.3 Numerical model

The governing equations for the numerical model are equations (1) and (2) as well as a predefined relation between fluid pressure, P, and total density, ρ_{total} (black line in Fig 2a and e). This ρ_{total} versus P relation is a thermodynamic relation and can be determined for specific reactions from equilibrium phase calculations using open-access software such as PerpleX (Connolly, 1990, 2005) or Thermolab (Vrijmoed and Podladchikov, 2022) under the assumption that P corresponds to the thermodynamic pressure (e.g., Mazzucchelli et al., 2024, 2026). We term such thermodynamic relation a look-up table because for a given ρ_{total} this look-up table provides a unique value of P. We solve equations (1) and (2) with the finite difference method and an explicit first-order time integration scheme (e.g., Patankar, 2018).

For the 1D model configuration, the ambient fluid pressure, P_{amb}, is everywhere equal to the thermodynamic pressure at which the (de)volatilization reaction occurs except at the left model boundary where the fluid pressure has a perturbation, P_{per} (Fig. 2b and f). For dehydration simulations, $P_{\mathrm{per}} < P_{\mathrm{amb}}$ and for hydration simulations $P_{\mathrm{per}} > P_{\mathrm{amb}}$ (Fig. 2b and f). We present a dimensionless fluid pressure by subtracting P_{amb} from P and then dividing the difference by P_{per} so that

https://doi.org/10.5194/egusphere-2026-3107
Preprint. Discussion started: 15 June 2026

pressure values range between -1 and 0 for dehydration (Fig. 2b) and 0 and 1 for hydration (Fig. 2f). We also employ a dimensionless horizontal coordinate, x/L_c, where x is the horizontal distance and L_c is here an arbitrary characteristic length. For a dehydration simulation, the total density, ρ_{total}, is initially everywhere the density of the not-dehydrated rock except at the left model boundary where ρ_{total} is smaller and corresponds to the dehydrated rock (Fig. 2c). For the dehydrated rock, ρ_{total} can be smaller than for the not-dehydrated rock because the dehydration creates porosity and ρ_{total} must increase with increasing P due to thermodynamic stability (e.g., Landau and Lifshitz, 1980). For a hydration simulation, ρ_{total} is initially everywhere the density of the not-hydrated rock except at the left model boundary where ρ_{total} is larger and corresponds to the hydrated rock (Fig. 2g). We also present ρ_{total} in a dimensionless form by dividing it by ρ_{fluid}. Within the time loop in the numerical algorithm, P is calculated from ρ_{total} using the look-up table and subsequently the new ρ_{total} is calculated from equations (1) and (2). We employ a dimensionless k/η = 1 (which means that the k/η used in the simulation is the real dimensional value of k/η divided by itself) and use as characteristic time, t_c, the arbitrary duration of the simulation. During the numerical (de)hydration simulations, the time evolution of the reaction front, x_{front} (Fig. 2c), is recorded for both dehydration (Fig. 2d) and hydration (Fig. 2h).

We also perform two simulations with the numerical model of Schmalholz et al. (2024) (the algorithm is available under https://doi.org/10.5281/zenodo.11129250.). Their model is based on three equations: the conservation equation for total mass, the conservation equation for the non-volatile solid mass (e.g. SiO or MgO which always are bound in the solid and are not dissolved in the fluid) and Darcy's law including a nonlinear Carman-Kozeny porosity-permeability relation. The model employs also a look-up table, but not between ρ_{total} and P, instead between P and the fluid and solid densities as well as the product of solid density and mass fraction of the immobile solid mass. These three look-up tables are employed as parameterised relation (equations 28 and 29 in Schmalholz et al. (2024)). The model is more elaborated because the spatial and temporal evolution of porosity, φ, is calculated and used in the Carman-Kozeny porosity-permeability relation. Also, the look-up table is smoothed so that the ρ_{total} versus P relation does not exhibit sharp corners as in the new numerical model presented here. The look-up table in the original model of Schmalholz et al. (2024) is adjusted so that it exhibits the same reaction-controlled variation in ρ_{total} as used in the numerical model of this study (section 2.1).

3 Results

3.1 Comparison of analytical and numerical solutions for a single reaction front

We compare the analytical solution for single-front propagation presented in section 2.1 with the numerical solution of the model described in section 2.3 and with the numerical solution for (de)hydration front propagation presented in Schmalholz et al. (2024). We calculate the time evolution of x_{front} using the analytical solution presented in equation (17). We calculate D_{eff} from the applied numerical values: $\Delta\rho_{\text{total}}$ is the absolute value of the difference between ρ_{total} at the left and right model boundary, ΔP is the absolute value of the difference between P at the left and right model boundary and k/η = 1.

The analytical solution and the two numerical models show essentially identical evolutions of the reaction front with progressive time for dehydration (Fig. 2d) and hydration (Fig. 2h) scenarios. The spatial profiles of P are similar for the two

https://doi.org/10.5194/egusphere-2026-3107
Preprint. Discussion started: 15 June 2026

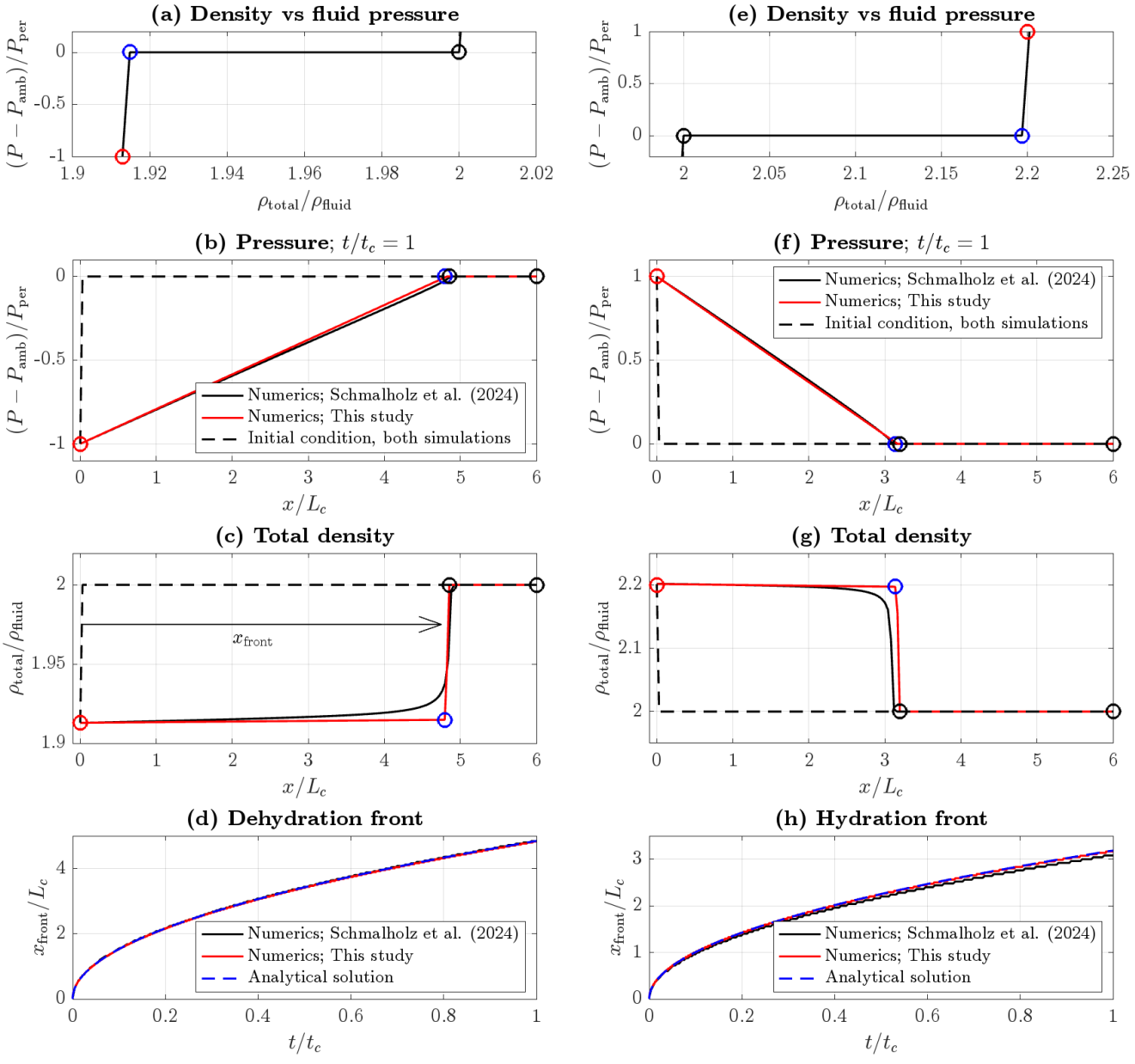

Figure 2. Analytical and numerical solutions for the propagation of pressure-controlled dehydration (panels a to d) and hydration fronts (panels e to h). All axes show dimensionless ratios (symbols are explained in the text). Panels a) and e) show the employed thermodynamic relation (or look-up table) between fluid pressure, P, and total density, ρ_{total}. The colored circles indicate the corresponding location of P and ρ_{total} values in the 1D model domain for P in panels b) and f) and for ρ_{total} in panels c) and g). Panels b) and f) show the spatial fluid pressure profile at the end of the simulations and c) and g) the corresponding total density profile. Legend in panels b) and f) also apply to c) and g). Panels d) and h) show the evolution of the position of the reaction front, x_{front}, versus time, t. Numerical results have been obtained with the model presented in this study and the model of Schmalholz et al. (2024), and the analytical solution is given in equation (17) (see legends).

https://doi.org/10.5194/egusphere-2026-3107
Preprint. Discussion started: 15 June 2026

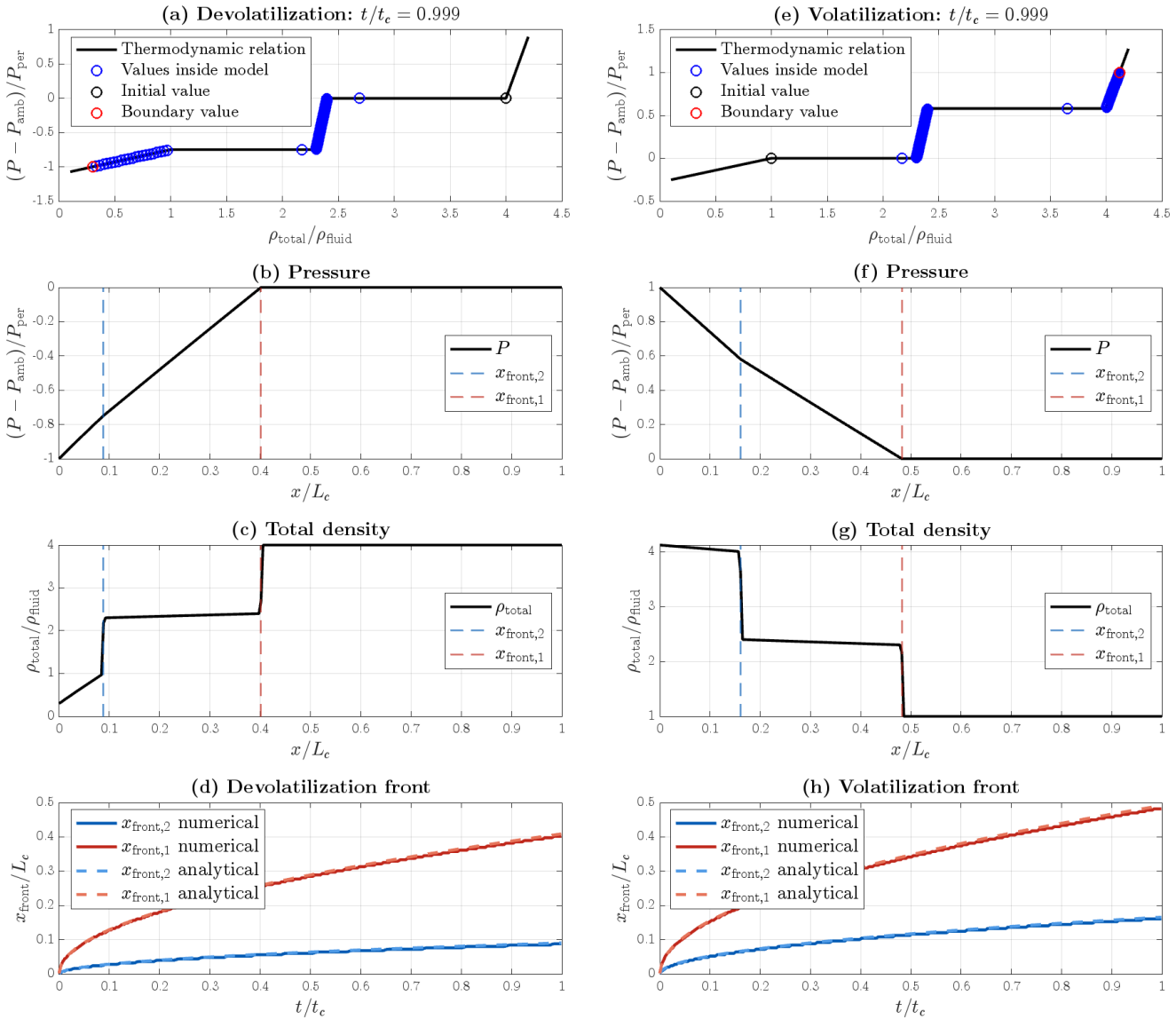

Figure 3. Comparison of numerical and analytical solutions for two propagating reaction fronts during devolatilization (left column) and volatilization (right column). The black lines in panels a) and e) show the thermodynamic relations between P and ρ_{total}. Open black and red circles indicate the initial and boundary conditions, respectively. Blue open circles indicate values inside the model domain. Panels b) and f) show the spatial distribution of dimensionless fluid pressure as a function of normalized distance at the end of the simulation. Dashed blue and red vertical lines mark the positions of the first and second reaction front, respectively. Panels c) and g) show the spatial profile of dimensionless total density at the end of the simulation. Panels d) and h) compare the time evolution of the numerical front positions (solid lines) with the positions predicted by the analytical solution (dashed lines). Red lines correspond to the first front and blue lines to the second front.

https://doi.org/10.5194/egusphere-2026-3107
Preprint. Discussion started: 15 June 2026

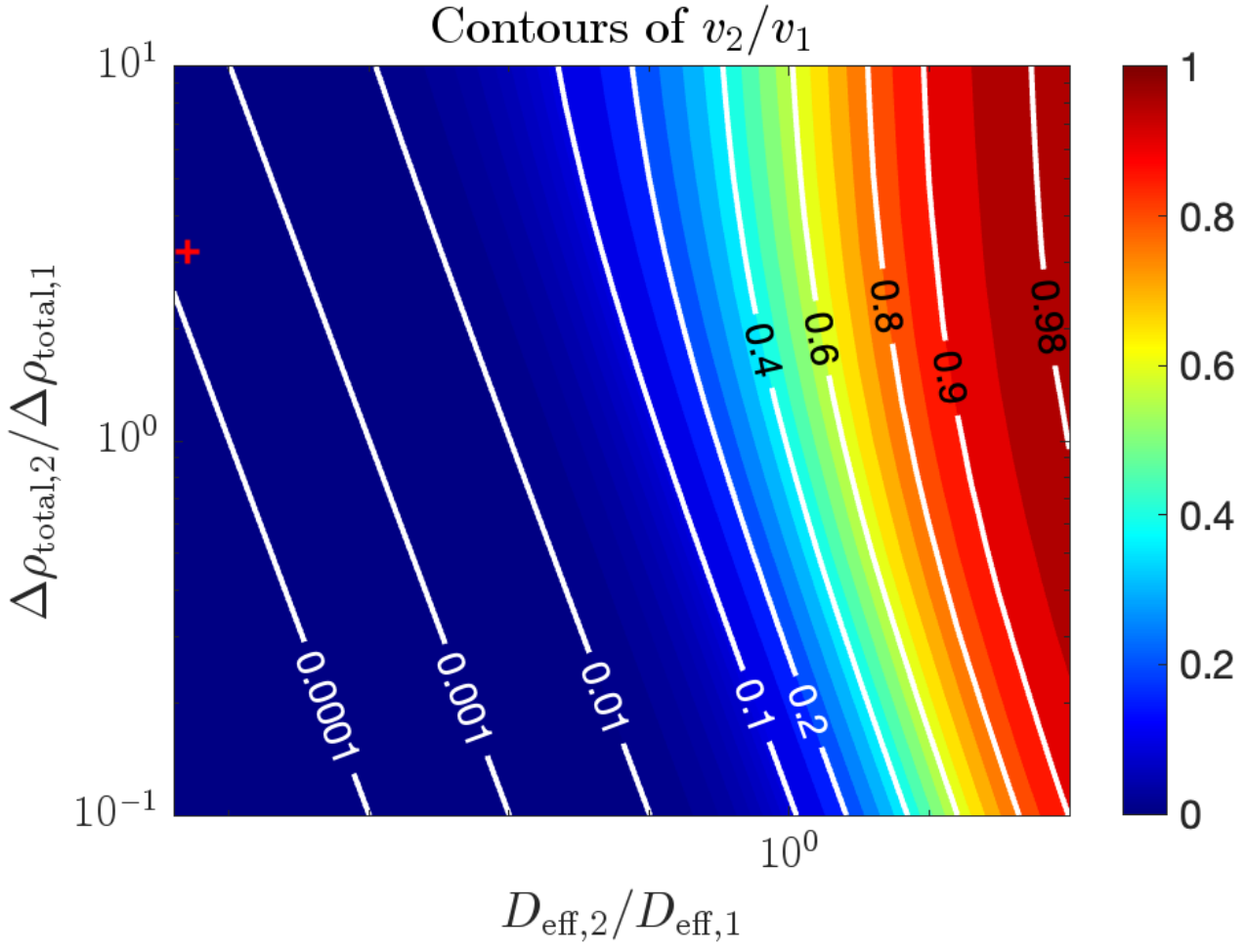

Figure 4. Results of the analytical solution for two coupled reaction fronts propagating in the same direction. The colored contour plot indicates the ratio of the two reaction front velocities, v_2/v_1 (equation 20), whereby v_1 is the velocity of the front that is ahead with respect to the propagation direction and v_2 is the velocity of the front that is behind (see also Fig. 3). $D_{\mathrm{eff},2}/D_{\mathrm{eff},1}$ is the ratio of the effective diffusivities for the respective fronts and $\Delta\rho_{\mathrm{total},2}/\Delta\rho_{\mathrm{total},1}$ is the ratio of the change in total density across the reaction for the respective fronts. The red plus sign indicates the values representative for a gypsum dehydration experiment discussed in section 4.4.

https://doi.org/10.5194/egusphere-2026-3107
Preprint. Discussion started: 15 June 2026

numerical simulations (Fig. 2b and f). The spatial profile of ρ_{total} shows a sharper front for the numerical model presented here compared to the model of Schmalholz et al. (2024) (Fig. 2c and g). The reason for this difference is that the model presented here employs a relation between ρ_{total} and P that is piecewise linear exhibiting sharp corners while the model of Schmalholz et al. (2024) employs a smoother relation between ρ_{total} and P. The reason for using either a sharp or smooth relation between ρ_{total} and P lies in the different solution strategies of the two numerical models: In the new model presented here, the unknown variable calculated numerically from the governing equation is ρ_{total} whereas P is determined by the look-up table, that is the predefined ρ_{total} versus P relation. Such strategy was already employed in the hydration model of Bras et al. (2023). In contrast, in the model of Schmalholz et al. (2024) P is calculated numerically from the governing PDE and ρ_{total} is determined from the look-up table. When ρ_{total} is the unknown, then variations of ρ_{total} across the reaction do not cause jumps in P since P is essentially constant across the reaction (Fig. 2a and e). In contrast, if P is the unknown, then small variations of P across the reaction cause large jumps in ρ_{total} and these jumps can cause numerical instabilities. To avoid these instabilities, the relation between P and ρ_{total} is smoothed when P is the unknown. The numerical model presented here is simplified since it only considers ρ_{total} and does not consider variations of ρ_{solid} and φ across the reaction. Nevertheless, the two numerical simulations provide the same evolution of the reaction front with time which also agree with the prediction of the analytical solution (Fig. 2d and h).

The agreement between the analytical solution and the results of the two numerical simulations (Fig. 2d and h) shows that the simplifications of a quasi-stationary moving front and a piecewise linear spatial profile of P are justified and do not cause significant deviations from the numerical solutions that do not involve these simplifications.

The advantage of the relation between ρ_{total} and P is that the analytical and numerical models can straightforwardly be elaborated to also simulate two different reaction fronts such as (de)volatilization reactions combined with phase transitions of the pore phase, as shown in the next section.

3.2 Solution for two coupled reaction fronts

We compare the analytical solution for two coupled reaction fronts with the numerical model described in section 2.3. The only difference between the numerical model for a single and two reaction fronts is the employed thermodynamic relation between P and ρ_{total}. For a single reaction there is only one region with a sharp jump in ρ_{total} that represents the reaction (Fig. 2a and e) whereas for two reactions there are two regions with a sharp jump in ρ_{total} (Fig. 3a and e). The spatial profile of P is more or less piecewise linear between the left model boundary and the first, rightmost reaction front (Fig. 3b and f). The profile of ρ_{total} shows two sharp jumps that represent two reactions (Fig. 3c and g). The two reaction fronts propagate with significantly different velocities whereby the first front propagates faster (Fig. 3d and h). The analytical and numerical solutions agree and predict identical relations between the positions of the two reaction fronts and the time (Fig. 3d and h).

The analytical solution shows that the two reaction fronts cannot propagate independently and that their propagation velocities are coupled. Using equations (A24) and (A27) shows that the ratio of the two propagation velocities is:

$$\frac{v_2}{v_1} = \frac{\lambda_2}{\lambda_1} = r. \tag{20}$$

https://doi.org/10.5194/egusphere-2026-3107
Preprint. Discussion started: 15 June 2026

The value of r is always between 0 and 1 and r depends on the effective diffusivities associated with the two reaction fronts and on the ratio of the total density change for each reaction. The fact that r is always between 0 and 1 shows that the second reaction front (having velocity v_2) propagating behind the first reaction front (having velocity v_1) is commonly slower and can never move faster than the first front that is ahead. These constraints on the velocity are due to the mass balance because the second front must not only balance the mass flux related to the second reaction but also the mass flux that is associated with the first front that propagates ahead. For example, if $D_{\mathrm{eff},2}/D_{\mathrm{eff},1}$ = 1 and $\Delta\rho_{total,2}/\Delta\rho_{total,1}$ = 1 then v_2/v_1 ≈0.4 (Fig. 4). Hence, even if both reactions exhibit the same effective diffusivities and the same change in total densities, the second front propagates with a velocity that is a factor of 0.4 slower than the velocity of the first front.

3.3 Effective diffusivity

The analytical solution for x_{front} (equation 17) can be written in the form

$$x_{\mathrm{front}} = \sqrt{2\,D_{\mathrm{eff}}\,t} = \sqrt{2\,\frac{\rho_{fluid}}{\Delta\rho_{total}}}\,\sqrt{\frac{k}{\eta}\,\Delta P\,t}. \tag{21}$$

Using in the analytical solution the same parameter values as used in the two numerical simulations shows that the evolution of x_{front} for both hydration and dehydration in the two numerical simulations agrees with the prediction of the analytical solution (Fig. 2d and h). The agreement between analytical and numerical solutions shows that the expression of D_{eff} governs (de)hydration front propagation.

Schmalholz et al. (2024) performed systematic numerical simulations of hydration front propagation and found the empirical relationship:

$$x_{\mathrm{front}} \approx 4\,\sqrt{\frac{k}{\eta}\,\Delta P\,t}. \tag{22}$$

In the systematic simulations of Schmalholz et al. (2024), the values in front of the square root ranged between 3 and 4.25 with most values close to 4. Schmalholz et al. (2024) did not have the new analytical solution derived here and did not explain the origin of this factor of 4. Comparing equations (21) and (22) indicates that if our analytically derived expression for x_{front} explains the empirically determined expression, one must have

$$\sqrt{2\,\frac{\rho_{fluid}}{\Delta\rho_{total}}} \approx 4. \tag{23}$$

The dimensionless values for densities used in the systematic simulations of Schmalholz et al. (2024) are ρ_{fluid} = 1 and $\Delta\rho_{\mathrm{total}}$ = 0.2. Hence, the value on the left side of equation (23) is ≈3.2, which is close to 4 and within the range of 3 and 4.25. The new analytical solution can, therefore, explain the factor of ≈4 in the empirical equation (22) which depends on the ratio of fluid density to total density change associated with the dehydration reaction.

https://doi.org/10.5194/egusphere-2026-3107
Preprint. Discussion started: 15 June 2026

4 Discussion

4.1 Hydraulic versus reaction-controlled effective diffusivity

In a non-reacting poroelastic medium, diffusion of fluid pressure is described by a parabolic PDE and governed by the hydraulic diffusivity, $D_{\mathrm{hyd}} = kK/\eta$, with k being the permeability, K a poroelastic modulus and η the fluid viscosity (e.g., Biot, 1941; Dutta and Ode, 1979; Wang, 2000; Shapiro et al., 2002). The hydraulic diffusivity governs the time scale at which pressure disturbances propagate, such that the characteristic distance of pressure disturbances grows with the square root of time. The expression for D_{hyd} is commonly derived for porous flow without reactions.

In our model, the mass balance at the moving (de)hydration front is described by the balance of two mass fluxes: a flux related to the reaction, quantified by $\Delta\rho_{\mathrm{total}}\, v_{\mathrm{front}}$, and a flux related to porous flow, quantified by $\rho_{\mathrm{fluid}}\, \varphi\, v_{\mathrm{fluid}}$ (equations 9 and 11, and Fig. 1). Fluid pressure diffusion is not a controlling process in the considered scenario, because ahead of the reaction front fluid pressure gradients are negligible and behind the front fluid pressure is close to equilibrium expressed by an approximately straight fluid pressure profile between the front and the drained model boundary (Fig. 1). Such fluid pressure behaviour in the regions behind and ahead of the reaction front was observed in numerical simulations of hydration and dehydration in Schmalholz et al. (2024). Our reactive model, considering fluid pressure-controlled (de)hydration reactions and associated density changes, also shows a relation between the propagation of fluid pressure disturbances from the left model side into the model domain and the square root of time. Substituting the equation for Darcy flux into the mass conservation equation and expressing ρ_{total} by P with a thermodynamic relation (Fig. 2a and e) yields a nonlinear diffusion-like equation for P, see also Schmalholz et al. (2024). However, in our simulations, the temporal evolution of P is linked to the evolution of the reaction front which is not controlled by the hydraulic diffusivity D_{hyd}, but by the effective, reaction-controlled diffusivity D_{eff} (Fig. 2).

To quantify the difference between D_{hyd} and D_{eff} we calculate the ratio $D_{\mathrm{eff}}/D_{\mathrm{hyd}}$ by modifying the expression for D_{eff}:

$$D_{\mathrm{eff}} = \frac{\rho_{\mathrm{fluid}}}{\Delta\rho_{\mathrm{total}}} \frac{k\,\Delta P}{\eta} = \frac{\rho_{\mathrm{fluid}}}{\Delta\rho_{\mathrm{total}}} \frac{\Delta P}{K} \frac{k\,K}{\eta} = \frac{\rho_{\mathrm{fluid}}}{\Delta\rho_{\mathrm{total}}} \frac{\Delta P}{K} D_{\mathrm{hyd}}. \tag{24}$$

Hence, we get

$$\frac{D_{\mathrm{eff}}}{D_{\mathrm{hyd}}} = \frac{\rho_{\mathrm{fluid}}}{\Delta\rho_{\mathrm{total}}} \frac{\Delta P}{K}. \tag{25}$$

The poroelastic modulus K does not vary significantly for different rocks and we assume here a representative value of 50 GPa (e.g., Karrech et al., 2018; Selvadurai and Suvorov, 2022). We consider seven ratios of $\rho_{\mathrm{fluid}}/\Delta\rho_{\mathrm{total}}$ that vary between 5 and 20 (Fig. 5), assuming ρ_{fluid} = 1000 kg/m^3, and using values for $\Delta\rho_{\mathrm{total}}$ that were suggested for several metamorphic reactions. The least constrained quantity is the fluid pressure difference, ΔP, driving the fluid flow and, hence, we consider here a wide range of ΔP between 0.1 and 100 MPa. The calculations of $D_{\mathrm{eff}}/D_{\mathrm{hyd}}$ show that D_{eff} is always significantly smaller than D_{hyd}, typically between two and four orders of magnitude (Fig. 5). Therefore, the timescales of the propagation of (de)volatilization fronts should not be calculated with D_{hyd} because the hydraulic diffusion timescales would underestimate

https://doi.org/10.5194/egusphere-2026-3107
Preprint. Discussion started: 15 June 2026

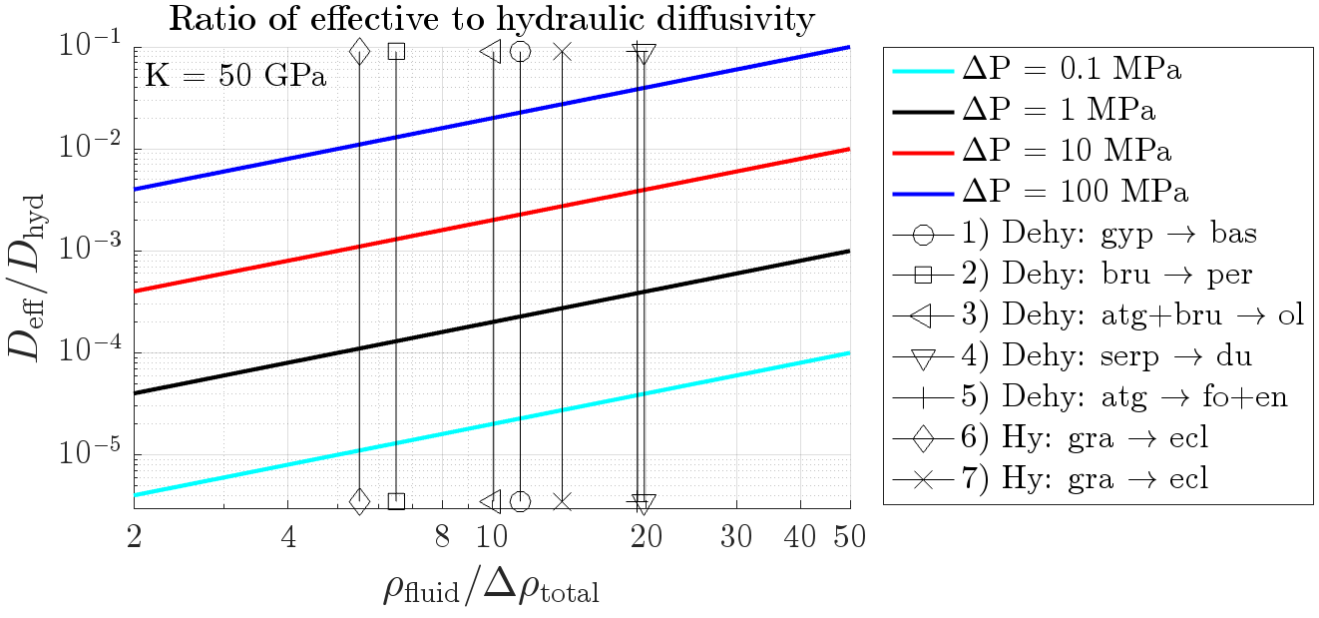

Figure 5. Ratio of effective to hydraulic diffusivity, $D_{\mathrm{eff}}/D_{\mathrm{hyd}}$, versus density ratio, $\rho_{\mathrm{fluid}}/\Delta\rho_{\mathrm{total}}$, for different values of the fluid pressure difference, ΔP, and a specific value for the poroelastic modulus, K (see equation 25). Vertical lines indicate representative values of $\rho_{\mathrm{fluid}}/\Delta\rho_{\mathrm{total}}$ for 1) dehydration of gypsum to bassanite (Fusseis et al., 2012), 2) dehydration of brucite to periclase (Schmalholz et al., 2020), 3) dehydration of antigorite + brucite to olivine (Schmalholz et al., 2023), 4) dehydration of serpentinite to dunite (Malvoisin et al., 2015), 5) dehydration of antigorite to forsterite + enstatite for a negative Clapeyron slope (Porkoláb et al., 2025), 6) hydration of granulite to eclogite (Bras et al., 2023), 7) hydration of granulite to eclogite (Centrella, 2019).

the real timescale by orders of magnitude. The timescale of (de)volatilization front propagation should, hence, be calculated with the reaction-controlled D_{eff}.

4.2 Reaction-controlled front retardation

Comparison of D_{eff} with D_{hyd} shows that in the presence of reactions propagating fluid pressure disturbances are retarded, or slowed down, compared to pure diffusive propagation without reactions. Hydraulic diffusion can be simulated with our numerical model by employing a linear relation between P and ρ_{total} for which P is monotoneously increasing with increasing ρ_{total} (Fig. 6). This linear relationship represents poroelasticity and the slope of the P versus ρ_{total} line represents the poroelastic modulus (Fig. 6d). A reaction associated with a change in ρ_{total} modifies the relation between P and ρ_{total} because across the reaction P remains constant while ρ_{total} increases (Fig. 6e). Such sharp density change represents an univariate reaction. The reaction retards the propagation of pressure disturbances because while ρ_{total} is changing across the reaction the values of P do not not change and, hence, disturbances of P do not propagate (Fig. 6). Similarly, the reaction front can be further retarded when a second front is added to the system and propagates behind the first front (Fig. 6).

https://doi.org/10.5194/egusphere-2026-3107
Preprint. Discussion started: 15 June 2026

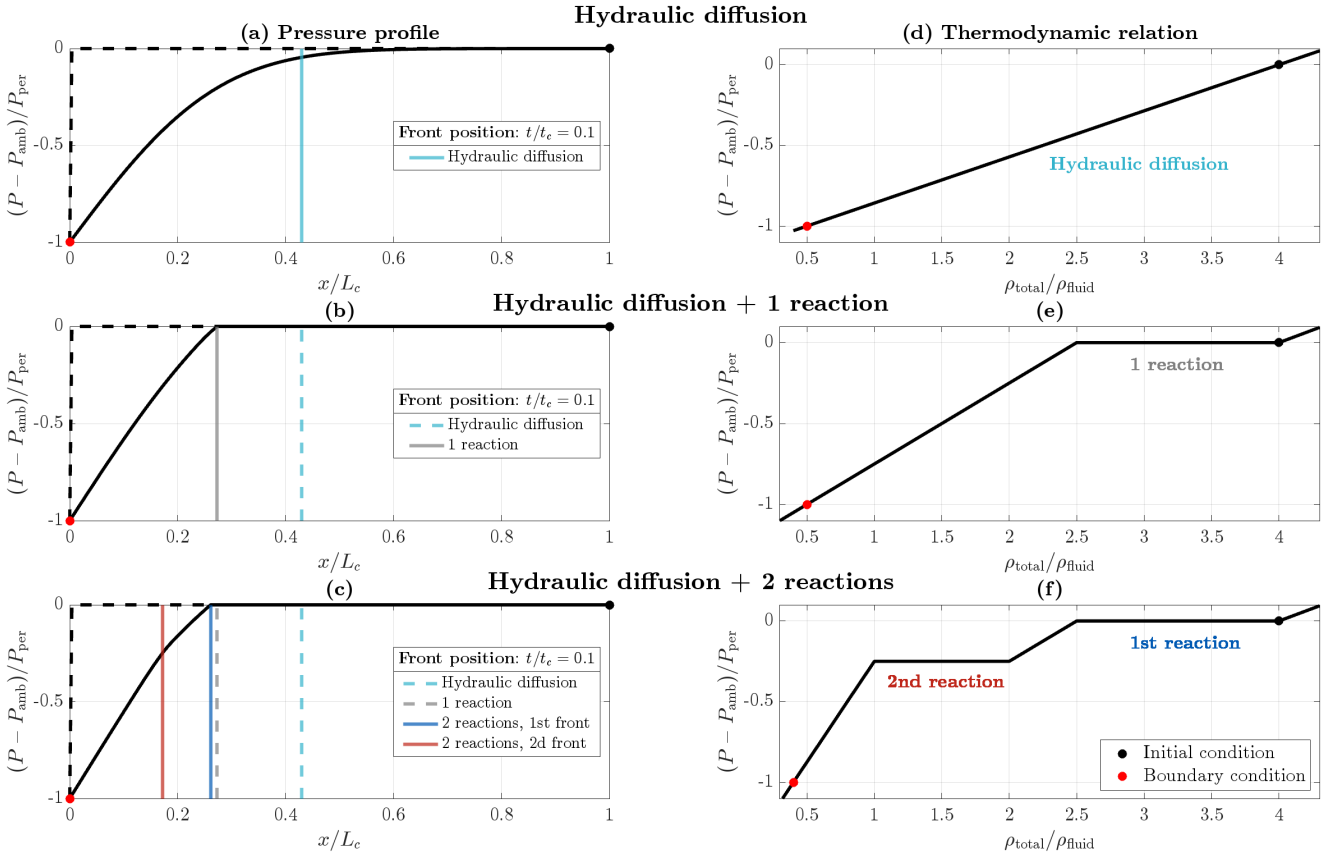

Figure 6. Numerical solutions of the free-boundary diffusion problem for pure hydraulic diffusion and for cases involving one and two consecutive devolatilisation reactions. The figure illustrates how devolatilisation reactions retard the propagation of a pressure-driven front relative to the purely hydraulic case. The left column shows pressure profiles as a function of normalized distance, x/L_c, whereas the right column shows the constitutive relations $P(\rho_{\text{total}})$ that encode the phase assemblages and reaction thresholds. In the absence of reactions (top row), the perturbation propagates diffusively and reaches the largest distance. With one devolatilisation reaction (middle row), part of the perturbation is absorbed at the reaction threshold, reducing the propagation distance. With two consecutive devolatilisation reactions (bottom row), the perturbation is distributed across two phase transitions, producing two reaction fronts and a stronger retardation effect. The figure therefore provides a conceptual interpretation of the numerical solutions and demonstrates how successive devolatilisation reactions alter the effective propagation distance and time scale of pressure-front migration.

https://doi.org/10.5194/egusphere-2026-3107
Preprint. Discussion started: 15 June 2026

The slowing of a (de)volatilization front due to reaction-induced changes in ρ_{total} is analogous to the retardation of temperature-controlled phase-transition fronts, such as the freezing of a water column or the solidification of a magma lake (e.g., Stefan, 1891; Turcotte and Schubert, 2014). In these cases, the temperature remains constant during the phase change while thermal energy is either absorbed or released; the energy involved in maintaining this constant temperature is the latent heat (e.g., Turcotte and Schubert, 2014).

4.3 Permeability and timescales

The permeability, k, is an important parameter for the propagation of (de)volatilization fronts but commonly difficult to quantify. However, for some processes the values of $D_{\mathrm{eff}} = x^2_{\mathrm{front}}/t$ can be directly determined in laboratory experiments or estimated from field studies if the distance a reaction front has propagated can be dated. For such cases, k can be estimated using relations in equation (24) with the equation:

$$k = \frac{\eta}{2\,\Delta P}\frac{\Delta\rho_{total}}{\rho_{fluid}}\frac{x^2_{\mathrm{front}}}{t}. \tag{26}$$

We use the values of x^2_{front}/t determined for three naturally observed and dated reaction fronts, which all are between 4×10^{-11} and 10^{-8} $\mathrm{m^2 s^{-1}}$ (Fig. 7a). Using again a wide range of values for ΔP and representative values for $\rho_{\mathrm{fluid}}/\Delta\rho_{\mathrm{total}}$ and η shows that k ranges between 10^{-18} and 10^{-24} $\mathrm{m^2}$ (Fig. 7a). The large variation in estimates of k results from the large variation in ΔP we have applied. Nevertheless, the estimated range of k agrees with independent estimates of permeability for porous flow processes for confining pressures that represent the deep crust or subduction plate interface. For example, Ingebritsen and Manning (2010) estimate k to range between 10^{-16} and 10^{-18} $\mathrm{m^2}$ for deep crustal rocks. Based on seismological observations of unusually high Vp/Vs regions, Peacock et al. (2011) estimate the permeability of the subduction plate interface to range between 10^{-24} and 10^{-21} $\mathrm{m^2}$. Laboratory measurements of k provide values between 10^{-18} and 10^{-21} $\mathrm{m^2}$ for low-temperature serpentinite at 100 MPa confining pressure (Hatakeyama et al., 2017). Extrapolations of the laboratory results indicate that these values of k further decrease several orders of magnitude for larger confining pressures (Hatakeyama et al., 2017). Very low values of $k < 10^{-22}$ $\mathrm{m^2}$ were also proposed based on field observations of vugs (Angiboust and Raimondo, 2022) and of fluid veins that were present across the blueschist-to-eclogite transition (Strobl et al., 2025). The order-of-magnitude agreement between estimates of k based on our new analytical solution for (de)hydration front propagation and independent laboratory measurements and field observations suggests that many (de)volatilization reactions at lower crustal and sub-crustal levels occur for a range of k between 10^{-18} and 10^{-24} $\mathrm{m^2}$.

Assuming representative parameters, the timescale for the propagation of a (de)volatilization front can be estimated (Fig. 7b). The larger the change in total density associated with the reaction the longer it takes for the reaction front to propagate a certain distance. For representative metamorphic (de)hydration reactions the timescale to generate a reaction front with a witdth of 1 m varies by a factor of ≈5 due to the different magnitude of density change associated with the different reactions (Fig. 7b). For representative quantities, the timescale to generate a reaction front of 1 m width is in the order of 10 years (Fig. 7b). Clearly, this timescale can vary significantly if the representative quantities are varied significantly. Nevertheless, the advantage

https://doi.org/10.5194/egusphere-2026-3107
Preprint. Discussion started: 15 June 2026

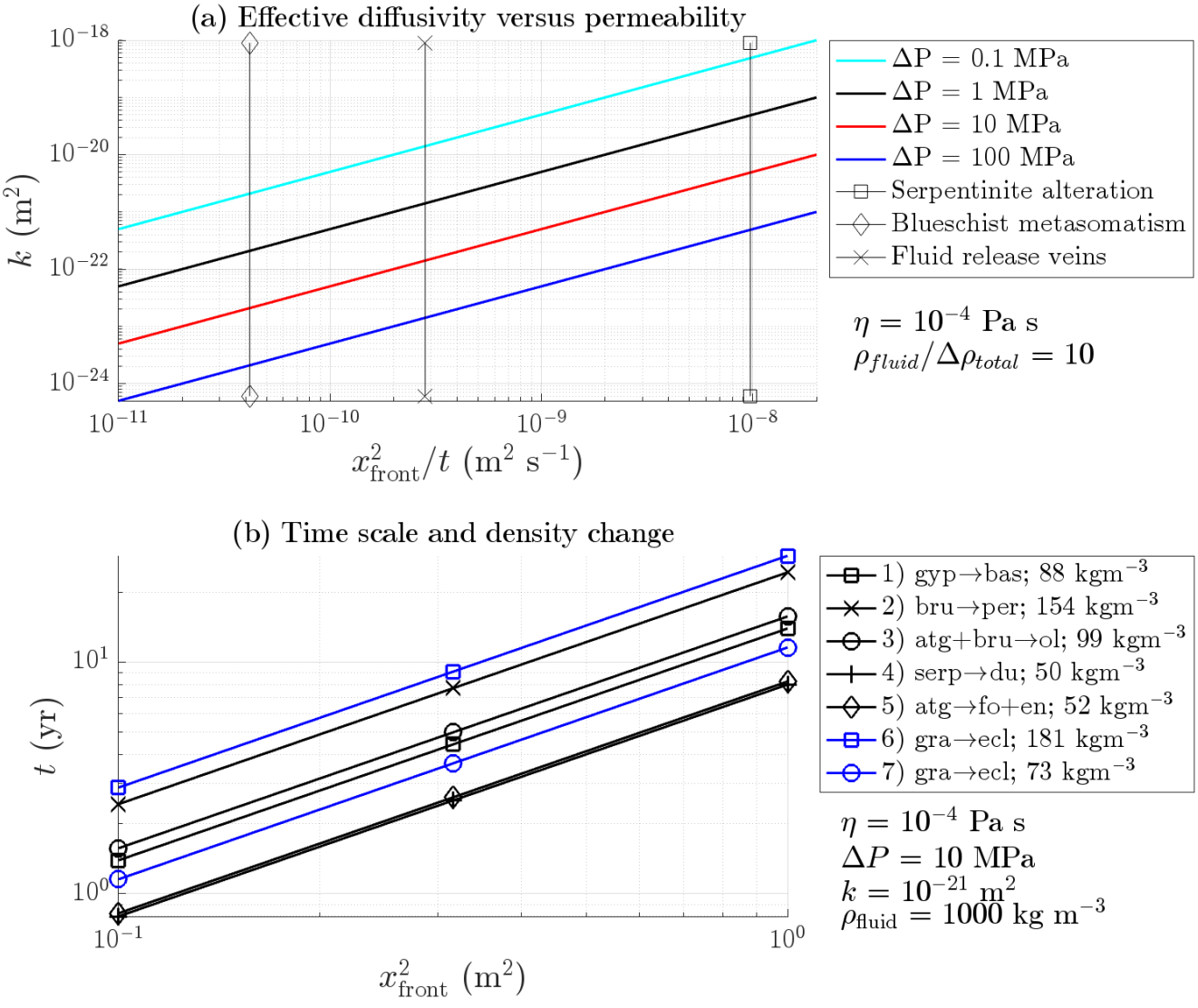

Figure 7. Panel a) shows relationship between permeability, k, and effective diffusivity of reaction front propagation, x^2_{front}/t, based on equation (26). Representative diffusivity values for serpentinite alteration are from Beinlich et al. (2020), blueschist metasomatism from John et al. (2012) and fluid release veins from Taetz et al. (2018). b) Impact of (de)hydration-induced change in total density on the duration, t, required to generate a (de)hydration zone with a width of x_{front}. Note that the graph shows the relation between t and x^2_{front}. The legend refers to the same reactions specified in the caption of figure 4 and the displayed density values quantify the corresponding total density change.

of the new analytical solution is that it allows to estimate the timescale of the progression of natural (de)volatilization processes because it captures both governing processes of reaction-induced density changes and porous fluid flow.

https://doi.org/10.5194/egusphere-2026-3107
Preprint. Discussion started: 15 June 2026

4.4 Application to published laboratory dehydration experiments

In many studies, the dehydration of gypsum has been experimentally investigated because it is tractable to laboratory investigation and can serve as analogue to many metamorphic devolatilization reactions (e.g., Heard and Rubey, 1966; Miller et al., 2003; Fusseis et al., 2012; Llana-Fúnez et al., 2012; Leclère et al., 2018; Schrank et al., 2020, 2021). Compared to experimental gypsum dehydration, our theoretical model is significantly simplified because we focus only on hydro-chemical processes and on macro-scale processes, such as density changes and porous flow. We ignore thermo-mechanical processes (e.g., Karrech et al., 2018), microstructural modifications accompanying gypsum's dehydration (e.g., Beaugnon et al., 2022) and reaction kinetics (e.g., Schrank et al., 2021). The main purpose of the applied simplifications is to get fundamental insight into the first-order hydro-chemical processes occuring during reaction front propagation as well as a study that does. Hence, we discuss in the following two experimental studies of gypsum dehydration that discuss the propagation of a dehydration front. Furthermore, we discuss a gypsum dehydration experiment that is governed by reaction kinetics and does not show a reaction front.

Based on laboratory gypsum dehydration experiments, Leclère et al. (2018) derived mathematical expressions for the distance and velocity of the dehydration front. In their analytical model, both the distance and the velocity of the dehydration front depend, amongst other parameters, on $\sqrt{k\Delta P/\eta}$. This dependency agrees with our model, since x_{front} also depends on $\sqrt{k\Delta P/\eta}$ (equation 21). Furthermore, we can calculate the velocity of the dehydration front from our solution for x_{front} which yields

$$v_{\text{front}} = \frac{dx_{\text{front}}}{dt} = \sqrt{\frac{2\,D_{\text{eff}}}{t}} = \sqrt{2\,\frac{\rho_{fluid}}{\Delta\rho_{total}}\,\frac{k\Delta P}{\eta}\,\frac{1}{t}}. \tag{27}$$

Therefore, in our model, v_{front} also depends on $\sqrt{k\Delta P/\eta}$ and our expressions for x_{front} and v_{front} show the same dependencies on $\sqrt{k\Delta P/\eta}$ as in the analytical results presented in Leclère et al. (2018). Leclère et al. (2018), however, do not provide an explicit relationship between front distance and square root of time and no expression for an effective diffusivity.

Fusseis et al. (2012) performed dehydration experiments with gypsum and showed the propagation of a dehydration front, using time-series synchrotron X-ray micro-tomography. The dehydration of gypsum formed bassanite and caused the propagation of a sharp porosity front (Fig. 8b). The average temporal evolution of the measured front distance scales with the square root of time. The representative diffusivity value that describes the experimental results is 8.29×10^{-11} m^2 s^{-1} (Fusseis et al., 2012). Based on the experimental observations and a later thermo-poro-mechanics modelling study (Karrech et al., 2018), it was suggested that this square root dependence results form the hydraulic diffusion of the fluid pressure (Fusseis et al., 2012; Karrech et al., 2018). To assess whether hydraulic diffusion can control dehydration front propagation, we estimate the order of magnitude of the required permeability. Using the expression for D_{hyd} with K = 50 GPa and $\eta = 3\times10^{-4}$ Pas as representative values for the experiment, a very low permeability of $k \approx 5\times10^{-25}$ m^2 is required to obtain the measured diffusivity of 8.29×10^{-11} m^{2}s^{-1} (Fig. 8a). The requirement of a low permeability can also be observed in the modelling study of Karrech et al. (2018) who used a porosity dependent permeability of the form $k = k_0\,(\varphi/\varphi_c)^n$ with $k_0 = 2\times10^{-21}$ m^2, φ_c = 20% and n = 6 for $\varphi < \varphi_c$. This formulation provides $k = 2\times10^{-26}$ m^2 for a porosity of 3%, $k = 3\times10^{-23}$ m^2 for a porosity of 10%

https://doi.org/10.5194/egusphere-2026-3107
Preprint. Discussion started: 15 June 2026

and $k = 4\times10^{-21}$ m^2 for a porosity of 30% (with $n = 2$ for $\varphi > \varphi_c$). Such permeability values seem very small for a measured porosity of ≈30% in the dehydrated region (Fig. 8a).

Based on our new analytical solution, we test an alternative explanation for the observed diffusivity in the dehydration experiment of Fusseis et al. (2012): The square root of time dependence of the dehydration front position results from the mass balance at the moving reaction front and, hence, D_{eff} (equation 24) controls the temporal evolution of the dehydration front and not D_{hyd}. We estimate the required permeability with D_{eff} and assume 1000 kgm^{-3} for the fluid density, and 2300 and 2700 kgm^{-3} for the solid densities of gypsum and bassanite, respectively. This provides $\Delta\rho_{total} \approx 100$ kgm^{-3} assuming an initial porosity of 3% in the gypsum before dehydration and a final porosity of 32% in the bassanite (Fig. 8b). Using further ΔP = 100 MPa as reported in Fusseis et al. (2012) yields $k = 10^{-23}$ m^2 from equation (26) (Fig. 8a). This permeability is also very low. Fusseis et al. (2012) report that they did not apply any confining pressure and that the sample was heated to 115 °C. Therefore, we suggest that around the sample boundaries the dehydrated water should have made a phase transition to vapor. If we assume that in the experiments the water-to-vapor front governed the measured front propagation, we can use the expression for D_{eff} with values for vapor to estimate k. This scenario would be possible, if the pore water pressure ahead of the vapor front would have been >≈53 MPa and would have inhibited the dehydration reaction because gypsum is stable at such pressures at 115 °C, as discussed by Fusseis et al. (2012). Such high pore fluid pressure could have been generated by internal stresses due to thermal expansion during heating of the gypsum sample (Karrech et al., 2018). At ≈100 °C, the transition of water to vapor is at $P \approx 0.14$ MPa and we assume $\Delta P = 0.14$ MPa. Furthermore, for vapor, we assume $\eta/\rho_{fluid} = 2.4\times10^{-5}$ m^{2}s^{-1} (the kinematic viscosity) and $\Delta\rho_{total} \approx 320$ kgm^{-3}. Using these values in equation (26) yields $k = 2.3\times10^{-18}$ m^2 (Fig. 8a). The estimated permeability associated with a vapor front is five orders of magnitude larger than the estimated permeability for the dehydration front.

We also apply our two-front solution to the dehydration experiment of Fusseis et al. (2012) and assume that the first reaction front is the dehydration of gypsum to form bassanite and the second front is the phase transition from dehydrated water to vapor. There are now two endmember possibilities: In the experiment, the gypsum dehydration front governed the propagation of the measured front and is associated to the measured diffusivity of 8.29×10^{-11} m^2 s^{-1}. Or, the water-to-vapor transition governed the measured front and this front is associated with the diffusivity of 8.29×10^{-11} m^{2}s^{-1}. We assume that the permeability is the same for the two reaction fronts. Assuming that the experimentally measured reaction front was governed by the dehydration front (that is x_1 in Appendix A) provides $k = 10^{-23}$ m^2, the same value as for the calculation considering a single dehydration front only (Fig. 8a). However, assuming that the experimentally measured reaction front was governed by the vapor-to-water front (that is x_2 in Appendix A) provides $k \approx 10^{-14}$ m^2 (Fig. 8a). This value is four orders of magnitude larger than the value for the single reaction front associated to the vapor-to-water transition. A value of $k = 10^{-14}$ m^2 is much more reasonable for a porosity of ≈30% than values of $k < 10^{-20}$ m^2 (e.g., Ehrenberg and Nadeau, 2005). For example, recent laboratory experiments of the dehydration of natural serpentinite measured a permeability between $k = 10^{-13}$ and 10^{-14} m^2 for a porosity of ≈30% in the region with olivine that resulted from serpentinite dehydration (Menzel et al., 2025).

Clearly, our solution is based on a simple hydro-chemical model and cannot capture all relevant thermo-hydro-mechanical-chemical processes that governed the gypsum dehydration experiment. Also, in the experiments, there was likely a diffuse

https://doi.org/10.5194/egusphere-2026-3107
Preprint. Discussion started: 15 June 2026

transition zone with a mixture of water and vapor having a complex 3D geometry. Nevertheless, based on our simple solution we suggest three alternative interpretations of the laboratory observations. First, the observed scaling of front position with the square root of time may result from a reaction-controlled effective diffusion process rather than from hydraulic diffusion. Second, the transition from pore water to pore vapor may strongly influence front propagation and could reconcile the observed high porosities of $\approx 30\%$ with permeabilities on the order of 10^{-14} m^2, which are consistent with such porosities. Third, because synchrotron X-ray microtomography measures density contrasts, the registered front may correspond to the density change of ≈ 320 kgm^{-3} due to the vapor-to-water transition rather than to the density change of ≈ 100 kgm^{-3} due to dehydration, even though dehydration is the process that controls the porosity increase. These interpretations could be tested in future studies using more advanced thermo-hydro-mechanical-chemical models that account for reaction-induced density changes and the water-to-vapor phase transition.

Whether or not a reaction front occurs in gypsum dehydration experiments depends on the applied experimental conditions. For example, Bedford et al. (2017) performed gypsum dehydration experiments with a confining pressure of 9 MPa, what avoids vaporization, and a lower fluid pressure of 4 MPa, which inhibits the fluid to drain out of the sample. In this experiment, no dehydration front was observed and dehydration reactions occurred initially only locally, producing grain-moat pairs evolving in relative isolation from nearby grains. The isolated pores caused high fluid pressures that hindered the dehydration reaction. With evolving time, the isolated pores connected more and more and dehydration progressed within patches of increasing size. The absence of a dehydration front in the experiment of Bedford et al. (2017) may also be explained by our solution, since the solution implies that a dehydration front propagates only when mass can be balanced across the moving reaction front which requires that the liberated water can freely flow away from the front (Fig. 1), which was not the case in the experiment.

Instead, Bedford et al. (2017) observed a progressive slowdown of reaction advance with time and attributed this deceleration to the observed coarsening: as bassanite grains grew and the fluid-filled moats surrounding them widened, diffusion paths for dissolved species increased, which progressively slowed the reaction. Such a slowdown may also be viewed within a broader coarsening framework. In materials science, coarsening commonly reflects the tendency of a system to reduce its total interfacial energy, which leads to a decrease in growth rate as the characteristic length scale increases. In the classical picture, this behavior is associated with a cube-root-of-time law for particle size. This process, known as coarsening or Ostwald ripening, is classically described by the LSW theory (Lifshitz and Slyozov, 1961). Similar behavior can also be reproduced within the Cahn–Hilliard framework, in which diffusion is coupled to interfacial energy effects, for example as discussed by Utkin et al. (2024). In addition, the deceleration may be linked to the progressive reduction of reactive specific surface area during coarsening, a mechanism that is well understood theoretically (Lasaga, 1998) and has been quantified in hydration experiments (Malvoisin et al., 2012). From this perspective, the slowdown reported by Bedford et al. (2017) may reflect not only diffusion across widening fluid-filled pore halos, but also the evolving coarsening geometry and the associated reduction in available reactive surface area. In addition, the experiments of Bedford et al. (2017) and Llana-Fúnez et al. (2012) document the dependence of gypsum dehydration rate on fluid pressure, in agreement with Lasaga's framework (Lasaga, 1998) assuming that the reactive rate is proportional to surface area and to the thermodynamic force such as overpressure over the equilibrium

https://doi.org/10.5194/egusphere-2026-3107
Preprint. Discussion started: 15 June 2026

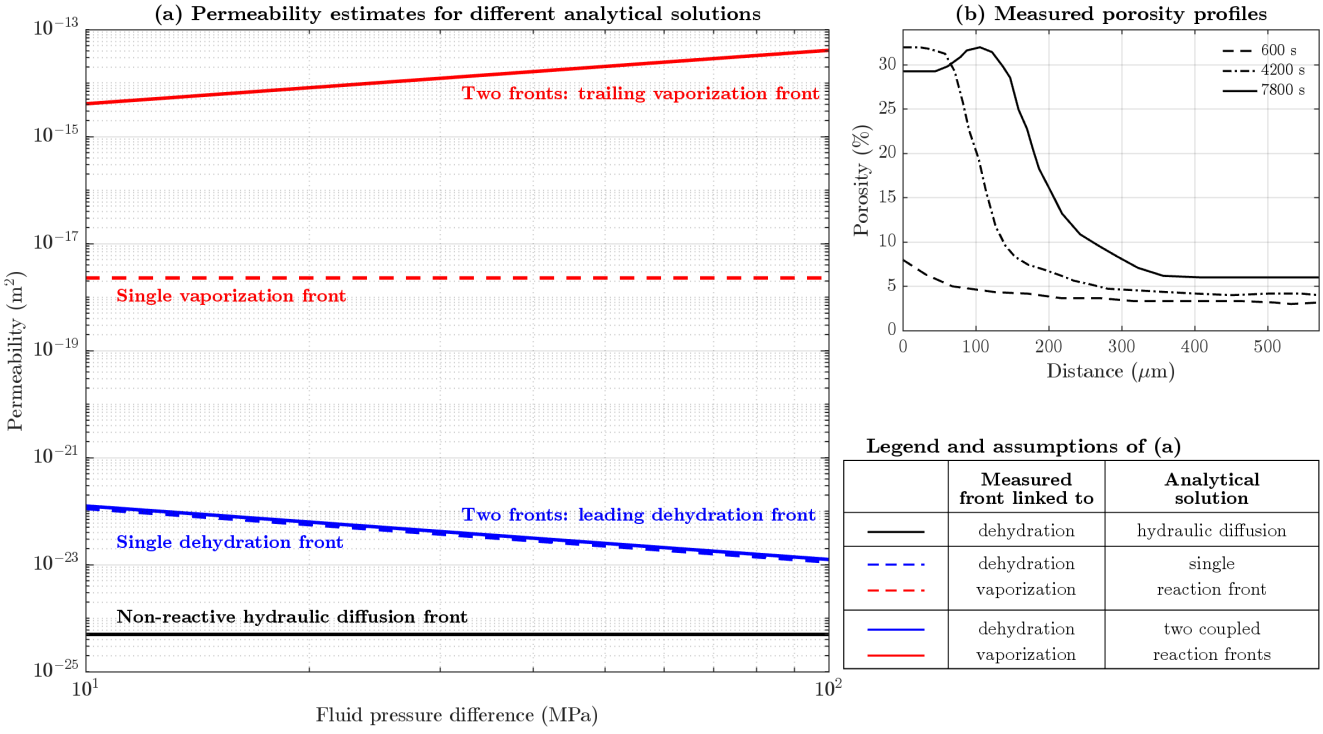

Figure 8. Panel (a): Permeability estimates, based on different analytical solutions and assumptions, for the gypsum dehydration experiment of Fusseis et al. (2012), and for a range of fluid pressure differences. The different lines represent different permeability estimates based on different analytical solution and on different assumption for the processes responsible for propagation of a sharp porosity fronts (panel b, redrawn after Fusseis et al. (2012)) measured in the experiments. The black line corresponds to a permeability estimate assuming that the porosity front is governed by hydraulic diffusion and that the porosity profile represents the dehydration front (see also legend). The blue dashed line corresponds to a permeability estimate based on our single front solution, assuming that the porosity profile represents the dehydration front. The red dashed line corresponds to a permeability estimate based on our single front solution, assuming that the porosity profile represents the vaporization front. The blue line corresponds to a permeability estimate based on our two-front solution, assuming that the porosity profile represents the first front due to dehydration. The red line corresponds to a permeability estimate based on our two-front solution, assuming that the porosity profile represents the second front due to vaporization. The applied solution and assumptions are summarized in the legend of (a). See text for more details of the permeability estimates.

425 reaction boundary. We plan to incorporate such reaction kinetics into our hydro-chemical models of reaction front propagation once kinetic laws are calibrated versus experimental data.

4.5 Analogy for chemically-controlled (de)volatilization reactions

In this study, we considered only pressure-controlled reactions, in which the total density change associated with the reaction is governed by variations in fluid pressure. However, metamorphic reactions can also be chemically controlled, such that the total

https://doi.org/10.5194/egusphere-2026-3107
Preprint. Discussion started: 15 June 2026

density change is driven by variations in the concentration of a chemical component (e.g., Huber et al., 2022). A prominent example is the dehydration of serpentinite, which can lead to the formation of different types of olivine veins. The formation of some olivine veins has been investigated in the context of pressure-controlled reactions (Schmalholz et al., 2023, 2024), whereas other vein types have been interpreted as the result of chemically controlled reactions (Huber et al., 2022).

Our analytical solution can also be applied to chemically-controlled reactions. Assuming that solid velocities and fluid pressure gradients are negligible, the 1D conservation equation for the total mass of a chemical element, such as silica, in a porous rock can be expressed by (e.g., Huber et al., 2022):

$$\frac{\partial \rho_{\mathrm{Ctotal}}}{\partial t} + \frac{\partial}{\partial x}\left[\rho_{\mathrm{fluid}}\,\varphi\, q_C\right] = 0, \tag{28}$$

where $\rho_{\mathrm{Ctotal}} = \rho_{\mathrm{fluid}}\, c_{\mathrm{fluid}}\, \varphi + \rho_{\mathrm{solid}}\, c_{\mathrm{solid}}\, (1-\varphi)$, with c_{fluid} and c_{solid} being concentrations of the chemical element in the fluid and solid, respectively, and q_C being the concentration diffusive flux (e.g., Huber et al., 2022):

$$q_C = -D_{\mathrm{C}} \frac{\partial c_{\mathrm{fluid}}}{\partial x}, \tag{29}$$

with D_{C} being a chemical diffusivity (e.g., Watson and Wark, 1997). Variations in c_{fluid} can trigger reactions associated with changes in total density in the same manner as variations in P (e.g., Huber et al., 2022). The governing equations for the pressure-controlled (equations 1 and 2) and chemically controlled (equations 28 and 29) models share the same mathematical structure. In both cases, the formulation consists of (i) a conservation equation and (ii) a flux equation. Furthermore, the quantity driving the flux, either P or c_{fluid}, is linked thermodynamically through a look-up table to the conserved quantity, ρ_{total} or ρ_{Ctotal}, respectively. More specifically, in the thermodynamic relationships shown in figure 2a and e, ρ_{total} is replaced by ρ_{Ctotal}, while the dimensionless pressure P on the vertical axis is replaced by c_{fluid}.

Assuming a thermodynamic relationship between c_{fluid} and ρ_{Ctotal} analogous to that between P and ρ_{total}, the same derivation used for pressure-controlled reaction front propagation can be applied to chemically controlled reactions. By analogy, this yields the following effective diffusivity for chemically controlled reactions:

$$D_{\mathrm{Ceff}} = \frac{\rho_{\mathrm{fluid}}\,\varphi}{\Delta\rho_{\mathrm{Ctotal}}}\, D_{\mathrm{C}}\, \Delta c_{\mathrm{fluid}}. \tag{30}$$

The effective diffusivity D_{Ceff} governs the propagation of (de)volatilization reaction fronts in systems where chemical diffusion of a component, such as silica, modifies its concentration and thereby triggers a reaction (e.g., Huber et al., 2022). By analogy with the analytical solution for the propagation of two coupled pressure-driven reaction fronts, D_{Ceff} and $\Delta\rho_{\mathrm{Ctotal}}$ can also be applied to obtain an analytical solution for the propagation of two chemically controlled reaction fronts.

4.6 Simplifications

(De)volatilization reactions can be triggered by changes in temperature, pressure, and chemical composition. In this study, we focus on hydro-chemical processes at the spatial scale of a reaction front, typically not exceeding a few tens of meters. At this scale, we neglect temperature gradients and heat transport. Furthermore, we do not consider mechanical deformation and its coupling with hydro-chemical processes, although mechanical effects may significantly influence the temporal and spatial

https://doi.org/10.5194/egusphere-2026-3107
Preprint. Discussion started: 15 June 2026

evolution of (de)volatilization processes (e.g., Karrech et al., 2018; Evans et al., 2020; Schmalholz et al., 2020, 2023). We also neglect reaction kinetics, which may depend on variables such as temperature, fluid content, or stress (e.g., Lasaga, 1998; Schrank et al., 2021; Eberhard et al., 2025). The primary motivation for these simplifications is to obtain closed-form analytical solutions for both single and coupled reaction-front propagation. Such analytical solutions provide a clear understanding of the considered hydro-chemical reaction front propagation. In contrast, more comprehensive models that account for fully coupled thermo-hydro-mechanical-chemical processes, as well as two- and three-dimensional geometries, typically require less transparent numerical approaches (e.g., Regenauer-Lieb et al., 2013; Poulet et al., 2014; Karrech et al., 2018; Evans et al., 2020; Schmalholz et al., 2023).

5 Conclusions

We present a new analytical solution describing the propagation of fluid pressure-driven (de)volatilization reaction fronts. The solution predicts that the width of the reaction zone increases proportionally to the square root of time. Importantly, this square-root dependence arises from mass balance across the moving reaction front rather than from hydraulic pore pressure diffusion. Front propagation is governed by an effective diffusivity that controls the timescales and spatial progression of (de)volatilization processes. This effective diffusivity depends on both hydraulic and chemical parameters, including the fluid-pressure difference, permeability, viscosity of the pore-filling phase (fluid or vapor), and the total density change associated with the metamorphic reaction. It therefore differs fundamentally from the classical hydraulic diffusivity, which depends solely on hydraulic parameters and incorporates a poroelastic modulus instead of the fluid pressure difference. Moreover, conventional hydraulic diffusivity does not account for reaction-induced density changes and is typically substantially larger than the effective diffusivity derived here. The new analytical solution is in excellent agreement with numerical solutions of the governing equations, demonstrating that the simplifying assumptions adopted in the analytical derivation are appropriate.

We further elaborated the analytical solution for the simultaneous propagation of two coupled reaction fronts. This extended solution also agrees closely with numerical simulations. The analysis demonstrates that the two fronts cannot propagate independently because mass conservation requires coupling between the moving fronts. Consequently, the front located farther in the direction of propagation always advances more rapidly than the trailing front.

Application of the analytical solution to diffusivities inferred from natural rocks, together with density changes characteristic of common deep metamorphic reactions, yields permeability estimates ranging from 10^{-18} to 10^{-24} m^2. These values are consistent with independent permeability estimates obtained from laboratory experiments, seismological observations of high Vp/Vs regions and field observations of vugs and fluid veins.

Our analytical framework also provides a potential explanation for experimentally observed gypsum dehydration front propagation. For a porosity of approximately 30%, both the hydraulic diffusivity and the effective diffusivity associated with a single dehydration front require permeabilities smaller than 10^{-20} m^2 to reproduce the experimentally observed front diffusivities. In contrast, the two-front solution, which incorporates the transition from pore water to pore vapor near the sample boundaries, requires permeabilities on the order of 10^{-14} m^2, values that are likely more realistic for materials with porosities

https://doi.org/10.5194/egusphere-2026-3107
Preprint. Discussion started: 15 June 2026

of approximately 30%. Although the analytical treatment is necessarily simplified and natural dehydration processes are considerably more complex, the two-front solution highlights the importance of accounting for water-to-vapor phase transitions when interpreting dehydration experiments involving vaporization.

The analytical framework can also be extended to chemically controlled reactions in cases where transport occurs exclusively by chemical diffusion, without simultaneous porous fluid flow. Our solutions therefore define an effective diffusivity for both pressure-controlled and chemically controlled (de)volatilization processes involving propagating reaction fronts. A characteristic feature of propagating reaction fronts discovered in the derived analytical solution is the retardation effect of the reaction, that is the larger the density change due to the reaction the slower the reaction front propagates. The analytical solution provides a quantitative framework for estimating the timescales of natural (de)volatilization processes and for designing and interpreting laboratory experiments involving reaction-front propagation.

Code and data availability. All numerical results presented in this study have been generated by a self-developed numerical algorithm written in Matlab. The algorithms developed for this study will be made freely accessible once the manuscript would be accepted. The data for total density changes and effective diffusivities shown in figures 5 and 7, as well as the porosity profiles shown in figure 8b have been obtained from data published in the studies cited in the figure captions.

Appendix A: Approximate analytical solution for propagation of two sharp reaction fronts

We derive a quasi-stationary approximation for the propagation of two sharp reaction fronts using the same mass-balance approach as in the single-front scenario that we treated in section 2.1. We consider a two-phase medium consisting of a porous solid skeleton and a pore fluid. Hence, a reaction can occur in the solid, for example, the dehydration of serpentinite or gypsum, or in the fluid, for example, the transition from pore water to vapor. The following derivation provides approximate expressions for the front positions and clarifies the origin of the $\sqrt{t}$ scaling.

A1 Governing equation and geometry of the two-front problem

We consider the one-dimensional conservation law for total mass in the absence of diffusive fluxes and for negligible solid velocity:

$$\frac{\partial \rho_{\text{total}}}{\partial t} + \frac{\partial}{\partial x}\left(\rho_{\text{fluid}} q_D\right) = 0, \tag{A1}$$

with Darcy flux

$$q_D = -\frac{k}{\eta}\frac{\partial P}{\partial x}. \tag{A2}$$

We assume that the two-phase medium, consisting of a porous solid and a pore fluid or vapor, is separated into three regions by two sharp moving reaction fronts associated with two phase transitions (Fig. A1):

$$x = x_1(t), \qquad x = x_2(t), \qquad 0 < x_2(t) < x_1(t),$$

https://doi.org/10.5194/egusphere-2026-3107
Preprint. Discussion started: 15 June 2026

where $x_1(t)$ is the position of the first reaction front and $x_2(t)$ is the position of the second front.

The two reactions and the fluid flow are governed by the fluid pressure, P. We consider a scenario where the initial fluid pressure, P_{ini}, is equal everywhere to the reaction pressure of the first reaction, P_{F1}, except at the left model boundary where the fluid pressure, P_{LB}, is smaller than the reaction pressure of the second reaction, P_{F2} (Fig. A1), that is:

$$P_{LB} < P_{F2} < P_{F1} = P_{ini}. \tag{A3}$$

The model domain is, hence, decomposed into three regions which contain different phase assemblages, for example, bassanite and vapor, bassanite and water or gypsum and water. The spatial distribution of the three regions are (Fig. A1):

- region 0: $x > x_1(t)$,
- region 1: $x_2(t) < x < x_1(t)$,
- region 2: $0 < x < x_2(t)$

We denote the velocities of the two reaction fronts by

$$v_1(t) = \dot{x}_1(t), \qquad v_2(t) = \dot{x}_2(t). \tag{A4}$$

A2 Jump conditions at the two moving fronts

To derive the conditions at the two reaction fronts, we introduce, for each front separately, a moving coordinate frame:

$$z_1 = x - x_1(t), \qquad z_2 = x - x_2(t). \tag{A5}$$

For a front moving with velocity $v_j(t) = \dot{x}_j(t)$, $j = 1, 2$, the derivatives transform as

$$\frac{\partial}{\partial t}\Big|_x = \frac{\partial}{\partial t}\Big|_{z_j} - v_j(t)\frac{\partial}{\partial z_j}, \qquad \frac{\partial}{\partial x} = \frac{\partial}{\partial z_j}. \tag{A6}$$

Under the quasi-stationary approximation in the moving frame,

$$\frac{\partial}{\partial t}\Big|_{z_j} \approx 0, \tag{A7}$$

and equation (A1) can be written for the region closely around the front j,

$$-v_j(t)\frac{d\rho_{\text{total}}}{dz_j} + \frac{d}{dz_j}\left(\rho_{\text{fluid}} q_D\right) = 0, \tag{A8}$$

or, assuming that $v_j(t)$ is constant in space, equivalently,

$$\frac{d}{dz_j}\left[-v_j(t)\rho_{\text{total}} + \rho_{\text{fluid}} q_D\right] = 0. \tag{A9}$$

Therefore, the quantity in brackets is continuous across each reaction front, yielding the jump condition

$$\left[-v_j\rho_{\text{total}} + \rho_{\text{fluid}} q_D\right]\Big|_{z=z_{\text{j,behind}}} = \left[-v_j\rho_{\text{total}} + \rho_{\text{fluid}} q_D\right]\Big|_{z=z_{\text{j,ahead}}}, \qquad j = 1, 2, \tag{A10}$$

where the subscripts behind and ahead denote the values immediately behind and ahead of the corresponding front. Equations (A10) represent two jump conditions for two fronts, similar to the jump condition (equation 7) for a single front.

https://doi.org/10.5194/egusphere-2026-3107
Preprint. Discussion started: 15 June 2026

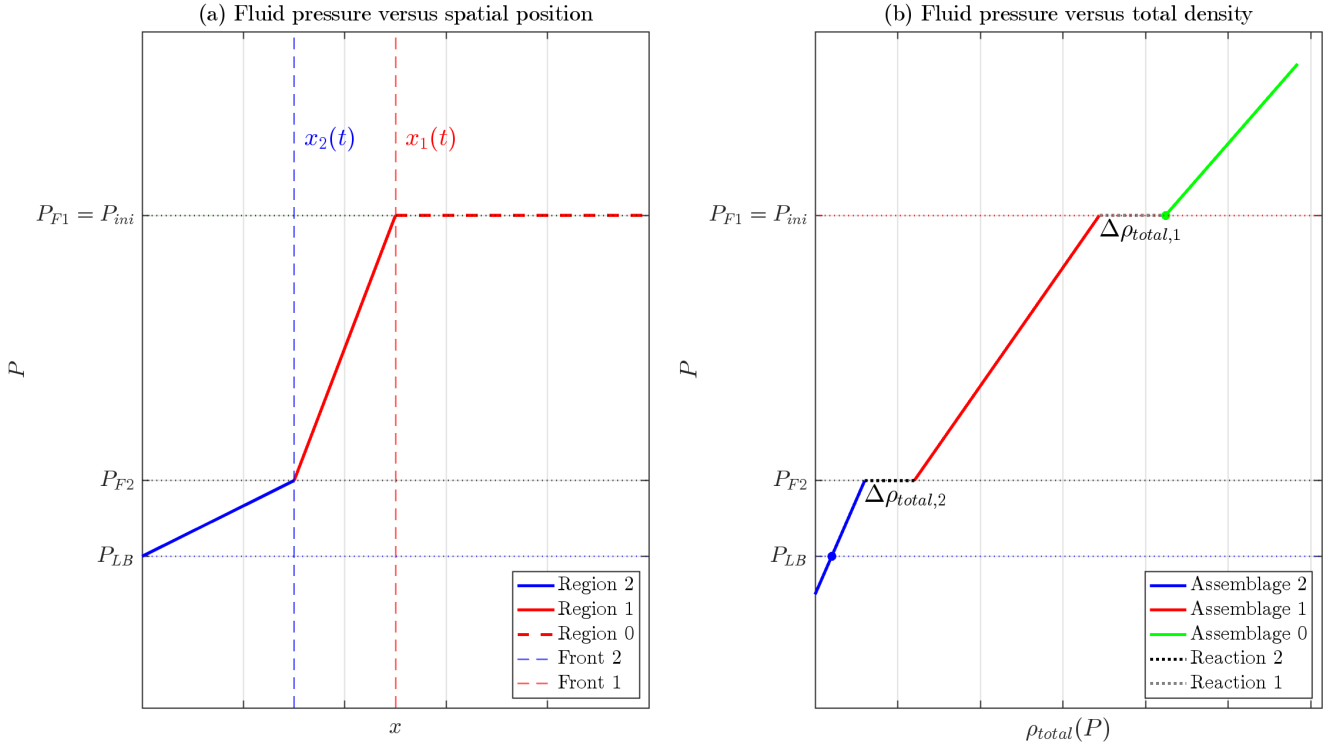

Figure A1. Schematic representation of the quasi-stationary two-reaction-front problem driven by fluid pressure P. The left panel shows the spatial distribution of fluid pressure, $P(x)$, at a representative instant of time, while the right panel shows the constitutive relation $\rho_{\text{total}}(P)$ represented as a piecewise linear function with two reaction-induced discontinuities corresponding to two phase transitions. Initially, the fluid pressure is uniform throughout the domain and equal to the reaction pressure of the second transition, $P_{ini} = P_{F1}$, except at the left boundary, where the imposed pressure satisfies $P_{LB} < P_{F2} < P_{F1}$. This boundary perturbation generates a pressure gradient and induces fluid flow from left to right. As a result, two moving reaction fronts emerge, located at $x_1(t)$ and $x_2(t)$, which separate three regions characterized by different phase assemblages: region 0 for $x > x_1(t)$, region 1 for $x_2(t) < x < x_1(t)$, and region 2 for $0 < x < x_2(t)$. The front at $x_1(t)$ marks the first reaction, activated when the pressure drops below P_{F1}, whereas the front at $x_2(t)$ marks the second reaction, associated with the threshold P_{F2}. This scheme also highlights the quantities entering the quasi-stationary derivation, namely the front positions, the pressure levels at the reaction thresholds, and the piecewise linear dependence of total density on pressure used to formulate the jump conditions at the two moving interfaces.

https://doi.org/10.5194/egusphere-2026-3107
Preprint. Discussion started: 15 June 2026

A3 Quasi-stationary approximation of the Darcy fluxes

To obtain a simple approximate solution for the reaction-front velocities, we assume that hydraulic equilibration inside regions 1 and 2 is much faster than the motion of the fronts. Therefore, the pressure profile in each region is approximated as quasi-stationary and linear. Let P_{LB} be the pressure imposed at the left boundary, $x = 0$, P_{F2} the reaction pressure at the second front, and P_{F1} the reaction pressure at the first front. Then the pressure gradients in regions 2 and 1 are approximated by

$$\left.\frac{\partial P}{\partial x}\right|_{\text{region 2}} \approx \frac{P_{F2} - P_{LB}}{x_2(t)}, \qquad \left.\frac{\partial P}{\partial x}\right|_{\text{region 1}} \approx \frac{P_{F1} - P_{F2}}{x_1(t) - x_2(t)}. \tag{A11}$$

Hence, the Darcy fluxes in regions 2 and 1 are

$$q_{D2} \approx -\frac{k_2}{\eta_2}\frac{\Delta P_2}{x_2(t)}, \tag{A12}$$

$$q_{D1} \approx -\frac{k_1}{\eta_1}\frac{\Delta P_1}{x_1(t) - x_2(t)}, \tag{A13}$$

where

$$\Delta P_2 = P_{F2} - P_{LB}, \qquad \Delta P_1 = P_{F1} - P_{F2} = P_{ini} - P_{F2}. \tag{A14}$$

For region 0, we adopt the same approximation as for the model with a single front and neglect the diffusive contribution ahead of the front located at x_1:

$$q_{D0} \approx 0. \tag{A15}$$

This assumption implies that the pore fluid transport associated with the propagation of both reaction fronts is supplied or extracted through the left model boundary across regions 2 and 1.

Substituting (A12)–(A15) into (A10) yields, for the second front at $x = x_2(t)$,

$$v_2 \Delta\rho_{\text{total},2} \approx \rho_{\text{fluid},2}\frac{k_2}{\eta_2}\frac{\Delta P_2}{x_2} - \rho_{\text{fluid},1}\frac{k_1}{\eta_1}\frac{\Delta P_1}{x_1 - x_2}, \tag{A16}$$

whereas for the first front at $x = x_1(t)$, we obtain

$$v_1 \Delta\rho_{\text{total},1} \approx \rho_{\text{fluid},1}\frac{k_1}{\eta_1}\frac{\Delta P_1}{x_1 - x_2}. \tag{A17}$$

Here, the corresponding density jumps across the two fronts are defined as

$$\Delta\rho_{\text{total},1} = \rho_{\text{total}}\Big|_{z=z_{1,\text{ahead}}} - \rho_{\text{total}}\Big|_{z=z_{1,\text{behind}}}, \qquad \Delta\rho_{\text{total},2} = \rho_{\text{total}}\Big|_{z=z_{2,\text{ahead}}} - \rho_{\text{total}}\Big|_{z=z_{2,\text{behind}}}. \tag{A18}$$

https://doi.org/10.5194/egusphere-2026-3107
Preprint. Discussion started: 15 June 2026

A4 Effective diffusivities and reaction-front velocities

In analogy with the single-front scenario, we define the effective diffusivities as

$$D_{\mathrm{eff},1} = \frac{\rho_{\mathrm{fluid},1}}{\Delta\rho_{\mathrm{total},1}} \frac{k_1}{\eta_1} \Delta P_1, \tag{A19}$$

$$D_{\mathrm{eff},2} = \frac{\rho_{\mathrm{fluid},2}}{\Delta\rho_{\mathrm{total},2}} \frac{k_2}{\eta_2} \Delta P_2. \tag{A20}$$

Using (A19)–(A20), equations (A16) and (A17) become

$$\dot{x}_2 = \frac{D_{\mathrm{eff},2}}{x_2} - \gamma \frac{D_{\mathrm{eff},1}}{x_1 - x_2}, \qquad \gamma = \frac{\Delta\rho_{\mathrm{total},1}}{\Delta\rho_{\mathrm{total},2}}, \tag{A21}$$

$$\dot{x}_1 = \frac{D_{\mathrm{eff},1}}{x_1 - x_2}. \tag{A22}$$

This coupled system of two equations governs the quasi-stationary dynamics of the two reaction fronts.

A5 Self-similar approximation

The structure of equations (A21) and (A22) is of the general form $\dot{x} \propto 1/x$ and, hence, suggests a $\sqrt{t}$ scaling (see equations 14 to 17). Therefore, we seek solutions of the form

$$x_1(t) = \lambda_1 \sqrt{t}, \qquad x_2(t) = \lambda_2 \sqrt{t}, \qquad 0 < \lambda_2 < \lambda_1. \tag{A23}$$

Then

$$\dot{x}_1 = v_1 = \frac{\lambda_1}{2\sqrt{t}}, \qquad \dot{x}_2 = v_2 = \frac{\lambda_2}{2\sqrt{t}}, \qquad x_1 - x_2 = (\lambda_1 - \lambda_2)\sqrt{t}. \tag{A24}$$

Substituting (A23)–(A24) into (A21)–(A22) and multiplying the resulting equations by $\sqrt{t}$ yields

$$\frac{\lambda_2}{2} = \frac{D_{\mathrm{eff},2}}{\lambda_2} - \gamma \frac{D_{\mathrm{eff},1}}{\lambda_1 - \lambda_2}, \tag{A25}$$

$$\frac{\lambda_1}{2} = \frac{D_{\mathrm{eff},1}}{\lambda_1 - \lambda_2}. \tag{A26}$$

Introducing the ratio

$$r = \frac{\lambda_2}{\lambda_1}, \qquad 0 < r < 1, \tag{A27}$$

we obtain

$$\lambda_2 = r\lambda_1, \qquad \lambda_1 - \lambda_2 = (1 - r)\lambda_1.$$

https://doi.org/10.5194/egusphere-2026-3107
Preprint. Discussion started: 15 June 2026

From equation (A26), it follows that

$$\lambda_1^2 = \frac{2D_{\mathrm{eff},1}}{1-r}. \tag{A28}$$

Substituting this relation into equation (A25), we obtain

$$D_{\mathrm{eff},1} r^2 + (D_{\mathrm{eff},2} + \gamma D_{\mathrm{eff},1})\, r - D_{\mathrm{eff},2} = 0. \tag{A29}$$

The physically admissible root satisfying $0 < r < 1$ is

$$r = \frac{-(D_{\mathrm{eff},2} + \gamma D_{\mathrm{eff},1}) + \sqrt{(D_{\mathrm{eff},2} + \gamma D_{\mathrm{eff},1})^2 + 4D_{\mathrm{eff},1} D_{\mathrm{eff},2}}}{2D_{\mathrm{eff},1}}. \tag{A30}$$

With r determined, we obtain

$$\lambda_1 = \sqrt{\frac{2D_{\mathrm{eff},1}}{1-r}}, \qquad \lambda_2 = r\lambda_1. \tag{A31}$$

Hence, the quasi-stationary approximation for the positions of the two reaction fronts is

$$x_1(t) = \lambda_1 \sqrt{t}, \qquad x_2(t) = \lambda_2 \sqrt{t}. \tag{A32}$$

The result (A32) shows that both fronts propagate proportionally to $\sqrt{t}$, as in the single-front scenario. However, unlike in the single-front case, the prefactors λ_1 and λ_2 are coupled because the trailing front at x_2 is controlled by both the mass flux entering region 2 and the mass flux transmitted into region 1, whereas the leading front at x_1 is controlled only by the mass flux through region 1.

The two-front quasi-stationary solution thus retains the same Stefan-like $\sqrt{t}$ scaling as the single-front scenario, but introduces a leading-order coupling between the front positions through the interval $x_1 - x_2$. In this sense, it provides the natural two-front extension of the approximate single-front relation (17):

$$x_{\mathrm{front}}(t) = \sqrt{2D_{\mathrm{eff}} t}, \qquad D_{\mathrm{eff}} = \frac{\rho_{\mathrm{fluid}}}{\Delta\rho_{\mathrm{total}}} \frac{k}{\eta} \Delta P.$$

Author contributions. L.K. developed the analytical solutions, implemented the model codes, performed the simulations and benchmarking, contributed to the interpretation of the results, and contributed to the manuscript preparation. S.M.S. contributed to the development of the model codes, performed model validation and benchmarking, contributed to the interpretation of the results, and contributed to the manuscript preparation. Y.P. contributed to the development of the model codes, the analytical investigation, and the interpretation of the results.

Competing interests. The authors declare that they have no conflict of interest.

Acknowledgements. S.M.S. thanks F. Fusseis for helpful discussions and useful information concerning gypsum dehydration experiments.

https://doi.org/10.5194/egusphere-2026-3107
Preprint. Discussion started: 15 June 2026

References

Aiki, T. and Muntean, A.: A free-boundary problem for concrete carbonation: Front nucleation and rigorous justification of the $t^{1/2}$-law of propagation, Interfaces and Free Boundaries, 15, 167–180, https://doi.org/10.4171/IFB/299, 2013.

Angiboust, S. and Raimondo, T.: Permeability of subducted oceanic crust revealed by eclogite-facies vugs, Geology, 50, 964–968, https://doi.org/10.1130/G50066.1, 2022.

Austrheim, H.: Eclogitization of lower crustal granulites by fluid migration through shear zones, Earth and Planetary Science Letters, 81, 221–232, https://doi.org/https://doi.org/10.1016/0012-821X(87)90158-0, 1987.

Beaugnon, F., Preturlan, J. G., Fusseis, F., Gouillart, E., Quiligotti, S., and Wallez, G.: From atom level to macroscopic scale: Structural mechanism of gypsum dehydration, Solid State Sciences, 126, 106 845, https://doi.org/https://doi.org/10.1016/j.solidstatesciences.2022.106845, 2022.

Bebout, G. E.: Chemical and Isotopic Cycling in Subduction Zones, in: Treatise on Geochemistry, edited by Holland, H. D. and Turekian, K. K., vol. 4, pp. 703–747, Elsevier, 2nd edn., https://doi.org/10.1016/B978-0-08-095975-7.00322-3, 2014.

Bedford, J., Fusseis, F., Leclère, H., Wheeler, J., and Faulkner, D.: A 4D view on the evolution of metamorphic dehydration reactions, Scientific Reports, 7, 6881, https://doi.org/10.1038/s41598-017-07160-5, 2017.

Beinlich, A., John, T., Vrijmoed, J. C., et al.: Instantaneous rock transformations in the deep crust driven by reactive fluid flow, Nature Geoscience, 13, 307–311, https://doi.org/10.1038/s41561-020-0554-9, 2020.

Biot, M. A.: General Theory of Three-Dimensional Consolidation, Journal of Applied Physics, 12, 155–164, https://doi.org/10.1063/1.1712886, 1941.

Brantut, N., Schubnel, A., David, E. C., Héripré, E., Guéguen, Y., and Dimanov, A.: Dehydration-induced damage and deformation in gypsum and implications for subduction zone processes, Journal of Geophysical Research: Solid Earth, 117, B03 205, https://doi.org/10.1029/2011JB008730, 2012.

Bras, E., Yamato, P., Schmalholz, S. M., Duretz, T., and Podladchikov, Y. Y.: Eclogitisation of dry and impermeable granulite by fluid flow with reaction-induced porosity: Insights from hydro-chemical modelling, Earth and Planetary Science Letters, 617, 118 256, https://doi.org/https://doi.org/10.1016/j.epsl.2023.118256, 2023.

Centrella, S.: The granulite-to eclogite- and amphibolite-facies transition: A volume and mass transfer study in the Lindås Nappe, Bergen arcs, west Norway, Geological Society, London, Special Publications, 478, 241–264, https://doi.org/10.1144/SP478.9, 2019.

Connolly, J.: Multivariable phase-diagrams: An algorithm based on generalized thermodynamics, American Journal of Science, 290, 666–718, 1990.

Connolly, J.: Devolatilization-generated fluid pressure and deformation-propagated fluid flow during prograde regional metamorphism, Journal of Geophysical Research: Solid Earth, 102, 18 149–18 173, https://doi.org/10.1029/97JB00731, 1997.

Connolly, J.: Computation of phase equilibria by linear programming: A tool for geodynamic modeling and its application to subduction zone decarbonation, Earth and Planetary Science Letters, 236, 524–541, https://doi.org/https://doi.org/10.1016/j.epsl.2005.04.033, 2005.

Coussy, O.: Poromechanics, John Wiley Sons, Chichester, England, ISBN 978-0-470-84920-0, https://onlinelibrary.wiley.com/doi/book/10.1002/0470092718, 2004.

Dahlen, F. A.: Metamorphism of nonhydrostatically stressed rocks, American Journal of Science, 292, 184–198, https://doi.org/10.2475/ajs.292.3.184, 1992.

https://doi.org/10.5194/egusphere-2026-3107
Preprint. Discussion started: 15 June 2026

Debret, B., Andreani, M., Muñoz, M., Bolfan-Casanova, N., Carlut, J., Nicollet, C., Schwartz, S., and Trcera, N.: Three steps of serpentinization in an eclogitized oceanic serpentinization front (Lanzo Massif–Western Alps), Journal of Metamorphic Geology, 31, 165–186, https://doi.org/10.1111/jmg.12008, 2013.

Dutta, N. C. and Ode, H.: Attenuation and dispersion of compressional waves in fluid-filled porous rocks with partial gas saturation (White model); Part I, Biot theory, Geophysics, 44, 1777–1788, https://doi.org/10.1190/1.1440938, 1979.

Eberhard, L., Mazzucchelli, M. L., Schmalholz, S. M., et al.: Coupling antigorite deformation and dehydration in high-pressure experiments, Contributions to Mineralogy and Petrology, 180, 64, https://doi.org/10.1007/s00410-025-02255-z, 2025.

Ehrenberg, S. N. and Nadeau, P. H.: Sandstone vs. Carbonate Petroleum Reservoirs: A Global Perspective on Porosity-Depth and Porosity-Permeability Relationships, AAPG Bulletin, 89, 435–445, https://doi.org/10.1306/10250404071, 2005.

Evans, O., Spiegelman, M., and Kelemen, P. B.: Phase-Field Modeling of Reaction-Driven Cracking: Determining Conditions for Extensive Olivine Serpentinization, Journal of Geophysical Research: Solid Earth, 125, e2019JB018 614, https://doi.org/https://doi.org/10.1029/2019JB018614, e2019JB018614 10.1029/2019JB018614, 2020.

Fowler, A. C.: A mathematical model of magma transport in the asthenosphere, Geophysical & Astrophysical Fluid Dynamics, 33, 63–96, https://doi.org/10.1080/03091928508245423, 1985.

Fusseis, F., Schrank, C., Liu, J., Karrech, A., Llana-Fúnez, S., Xiao, X., and Regenauer-Lieb, K.: Pore formation during dehydration of a polycrystalline gypsum sample observed and quantified in a time-series synchrotron X-ray micro-tomography experiment, Solid Earth, 3, 71–86, https://doi.org/10.5194/se-3-71-2012, 2012.

Galan, I., Andrade, C., Mora, P., and Sanjuan, M. A.: Sequestration of CO2 by Concrete Carbonation, Environmental Science & Technology, 44, 3181–3186, https://doi.org/10.1021/es903581d, pMID: 20225850, 2010.

Gupta, S. C.: The classical Stefan problem: basic concepts, modelling and analysis with quasi-analytical solutions and methods, vol. 45, Elsevier, 2017.

Hatakeyama, K., Katayama, I., Hirauchi, K.-i., and Michibayashi, K.: Mantle hydration along outer-rise faults inferred from serpentinite permeability, Scientific Reports, 7, 13 870, https://doi.org/10.1038/s41598-017-14309-9, 2017.

Heard, H. C. and Rubey, W. W.: Tectonic implications of gypsum dehydration, Geological Society of America Bulletin, 77, 741–760, 1966.

Huber, K., Vrijmoed, J. C., and John, T.: Formation of Olivine Veins by Reactive Fluid Flow in a Dehydrating Serpentinite, Geochemistry, Geophysics, Geosystems, 23, e2021GC010 267, https://doi.org/https://doi.org/10.1029/2021GC010267, e2021GC010267 2021GC010267, 2022.

Ingebritsen, S. E. and Manning, C. E.: Permeability of the continental crust: dynamic variations inferred from seismicity and metamorphism, Geofluids, 10, 193–205, https://doi.org/https://doi.org/10.1111/j.1468-8123.2010.00278.x, 2010.

John, T., Gussone, N., Podladchikov, Y., et al.: Volcanic arcs fed by rapid pulsed fluid flow through subducting slabs, Nature Geoscience, 5, 489–492, https://doi.org/10.1038/ngeo1482, 2012.

Kaatz, L., Schmalholz, S. M., and John, T.: Numerical Simulations Reproduce Field Observations Showing Transient Weakening During Shear Zone Formation by Diffusional Hydrogen Influx and H2O Inflow, Geochemistry, Geophysics, Geosystems, 24, e2022GC010 830, https://doi.org/https://doi.org/10.1029/2022GC010830, e2022GC010830 2022GC010830, 2023.

Karrech, A., Fusseis, F., Schrank, C., and Regenauer-Lieb, K.: Thermo-poro-mechanics Modelling of Gypsum Dehydration, in: Advances in Characterization and Analysis of Expansive Soils and Rocks, edited by Hoyos, L. R. and McCartney, J., pp. 177–188, Springer International Publishing, Cham, ISBN 978-3-319-61931-6, 2018.

Landau, L. D. and Lifshitz, E. M.: Statistical Physics, vol. 5 of *Course of Theoretical Physics*, Pergamon Press, Oxford, 3rd edn., 1980.

https://doi.org/10.5194/egusphere-2026-3107
Preprint. Discussion started: 15 June 2026

Lasaga, A. C.: Kinetic theory in the earth sciences, Princeton university press, 1998.

Leclère, H., Faulkner, D., Llana-Fúnez, S., Bedford, J., and Wheeler, J.: Reaction fronts, permeability and fluid pressure development during dehydration reactions, Earth and Planetary Science Letters, 496, 227–237, https://doi.org/https://doi.org/10.1016/j.epsl.2018.05.005, 2018.

Lifshitz, I. M. and Slyozov, V. V.: The kinetics of precipitation from supersaturated solid solutions, Journal of physics and chemistry of solids, 19, 35–50, 1961.

Liu, J.-H., Lanari, P., Tamblyn, R., Dominguez, H., Hermann, J., Rubatto, D., Forshaw, J. B., Piccoli, F., Zhang, Q. W., Markmann, T. A., Reynes, J., Li, Z. M., Jiao, S., and Guo, J.: Ultra-fast metamorphic reaction during regional metamorphism, Geochimica et Cosmochimica Acta, 394, 106–125, https://doi.org/https://doi.org/10.1016/j.gca.2025.01.036, 2025.

Llana-Fúnez, S., Wheeler, J., and Faulkner, D.: Metamorphic reaction rate controlled by fluid pressure not confining pressure: implications of dehydration experiments with gypsum, Contrib Mineral Petrol, 164, 69–79, https://doi.org/10.1007/s00410-012-0726-8, 2012.

Mainguy, M. and Coussy, O.: Propagation Fronts during Calcium Leaching and Chloride Penetration, Journal of Engineering Mechanics, 126, 250–257, https://doi.org/10.1061/(ASCE)0733-9399(2000)126:3(250), 2000.

Malvoisin, B., Brunet, F., Carlut, J., Rouméjon, S., and Cannat, M.: Serpentinization of oceanic peridotites: 2. Kinetics and processes of San Carlos olivine hydrothermal alteration, Journal of Geophysical Research: Solid Earth, 117, 2012.

Malvoisin, B., Podladchikov, Y. Y., and Vrijmoed, J. C.: Coupling changes in densities and porosity to fluid pressure variations in reactive porous fluid flow: Local thermodynamic equilibrium, Geochemistry, Geophysics, Geosystems, 16, 4362–4387, https://doi.org/https://doi.org/10.1002/2015GC006019, 2015.

Markmann, T. and Lanari, P.: Interplay Between Mechanical and Petrochemical Models on the Fluid Extraction From Subduction Zones, Journal of Metamorphic Geology, 44, 85–111, https://doi.org/https://doi.org/10.1111/jmg.70015, 2026.

Matter, J. M. and Kelemen, P. B.: Permanent storage of carbon dioxide in geological reservoirs by mineral carbonation, Nature Geoscience, 2, 837–841, https://doi.org/10.1038/ngeo683, 2009.

Mazzucchelli, M. L., Moulas, E., Kaus, B. J., and Speck, T.: Fluid-mineral Equilibrium Under Nonhydrostatic Stress: Insight From Molecular Dynamics, American Journal of Science, 324, 2, https://doi.org/10.2475/001c.92881, 2024.

Mazzucchelli, M. L., Moulas, E., Schmalholz, S. M., Kaus, B. J. P., and Speck, T.: Instability of Fluid-Mineral Equilibrium Under Non-Hydrostatic Stress Investigated With Molecular Dynamics, Journal of Geophysical Research: Solid Earth, 131, e2025JB033 520, https://doi.org/https://doi.org/10.1029/2025JB033520, e2025JB033520 2025JB033520, 2026.

Menzel, M. D., Eberhard, L., Arias, A., et al.: Controls of focused fluid release in subduction zones: insights from experimental dehydration of brucite vein networks in serpentinite, Contributions to Mineralogy and Petrology, 180, 30, https://doi.org/10.1007/s00410-025-02221-9, 2025.

Miller, S., van der Zee, W., Olgaard, D., and Connolly, J.: A fluid-pressure feedback model of dehydration reactions: experiments, modelling, and application to subduction zones, Tectonophysics, 370, 241–251, https://doi.org/https://doi.org/10.1016/S0040-1951(03)00189-6, physical Properties of Rocks and other Geomaterials, a Special Volume to honour Professor H. Kern, 2003.

Okazaki, K. and Hirth, G.: Dehydration of lawsonite could directly trigger earthquakes in subducting oceanic crust, Nature, 530, 81–84, https://doi.org/10.1038/nature16501, 2016.

Padrón-Navarta, J. A., Hermann, J., Garrido, C. J., López Sánchez-Vizcaíno, V., and Gómez-Pugnaire, M. T.: Metamorphic record of high-pressure dehydration of antigorite serpentinite to chlorite harzburgite in a subduction setting (Cerro del Almirez, Nevado–Filábride Complex, Southern Spain), Journal of Petrology, 52, 2047–2078, https://doi.org/10.1093/petrology/egr039, 2011.

https://doi.org/10.5194/egusphere-2026-3107
Preprint. Discussion started: 15 June 2026

Papadakis, V. G., Vayenas, C. G., and Fardis, M. N.: Experimental investigation and mathematical modeling of the concrete carbonation problem, Chemical Engineering Science, 46, 1333–1338, https://doi.org/https://doi.org/10.1016/0009-2509(91)85060-B, 1991a.

Papadakis, V. G., Vayenas, C. G., and Fardis, M. N.: FUNDAMENTAL MODELING AND EXPERIMENTAL INVESTIGATION OF CONCRETE CARBONATION, Materials, 88, 363–373, https://api.semanticscholar.org/CorpusID:138402924, 1991b.

Patankar, S.: Numerical Heat Transfer and Fluid Flow, CRC Press, https://doi.org/10.1201/9781482234213, 2018.

Peacock, S. M., Christensen, N. I., Bostock, M. G., and Audet, P.: High pore pressures and porosity at 35 km depth in the Cascadia subduction zone, Geology, 39, 471–474, https://doi.org/10.1130/G31649.1, 2011.

Pettke, T. and Bretscher, A.: Fluid-mediated element cycling in subducted oceanic lithosphere: The orogenic serpentinite perspective, Earth-Science Reviews, 225, 103 896, https://doi.org/10.1016/j.earscirev.2021.103896, 2022.

Philpotts, A. R. and Ague, J. J.: Principles of Igneous and Metamorphic Petrology, Cambridge University Press, 3 edn., 2022.

Porkoláb, K., Moulas, E., and Schmalholz, S. M.: Modeling the interplay between reaction progress, deformation and stress field evolution during antigorite dehydration: Implications for intermediate-depth seismicity, Geophysical Research Letters, 52, e2024GL113 865, https://doi.org/10.1029/2024GL113865, 2025.

Poulet, T., Veveakis, E., Regenauer-Lieb, K., and Yuen, D. A.: Thermo-poro-mechanics of chemically active creeping faults: 3. The role of serpentinite in episodic tremor and slip sequences, and transition to chaos, Journal of Geophysical Research: Solid Earth, 119, 4606–4625, https://doi.org/https://doi.org/10.1002/2014JB011004, 2014.

Putnis, A.: Mineral Replacement Reactions, Reviews in Mineralogy and Geochemistry, 70, 87–124, https://doi.org/10.2138/rmg.2009.70.3, 2009.

Raleigh, C. B. and Paterson, M. S.: Experimental Deformation of Serpentinite and Its Tectonic Implications, Journal of Geophysical Research, 70, 3965–3985, https://doi.org/10.1029/JZ070i016p03965, 1965.

Regenauer-Lieb, K., Veveakis, M., Poulet, T., Wellmann, F., Karrech, A., Liu, J., Hauser, J., Schrank, C., Gaede, O., Fusseis, F., and Trefry, M.: Multiscale coupling and multiphysics approaches in earth sciences: Applications, Journal of Coupled Systems and Multiscale Dynamics, 1, 49–73, https://doi.org/10.1166/jcsmd.2013.1003, 2013.

Schmalholz, S. M., Moulas, E., Plümper, O., Myasnikov, A. V., and Podladchikov, Y. Y.: 2D hydro-mechanical-chemical modeling of (de)hydration reactions in deforming heterogeneous rock: The periclase-brucite model reaction, Geochemistry, Geophysics, Geosystems, 21, e2020GC009 351, 2020.

Schmalholz, S. M., Moulas, E., Räss, L., and Müntener, O.: Serpentinite Dehydration and Olivine Vein Formation During Ductile Shearing: Insights From 2D Numerical Modeling on Porosity Generation, Density Variations, and Transient Weakening, Journal of Geophysical Research: Solid Earth, 128, e2023JB026 985, https://doi.org/https://doi.org/10.1029/2023JB026985, e2023JB026985 2023JB026985, 2023.

Schmalholz, S. M., Khakimova, L., Podladchikov, Y., Bras, E., Yamato, P., and John, T.: (De)hydration Front Propagation Into Zero-Permeability Rock, Geochemistry, Geophysics, Geosystems, 25, e2023GC011 422, https://doi.org/https://doi.org/10.1029/2023GC011422, e2023GC011422 2023GC011422, 2024.

Schmidt, M. W. and Poli, S.: Experimentally based water budgets for dehydrating slabs and consequences for arc magma generation, Earth and Planetary Science Letters, 163, 361–379, https://doi.org/10.1016/S0012-821X(98)00142-3, 1998.

Schrank, C. E., Gioseffi, K., Blach, T., Gaede, O., Hawley, A., Milsch, H., Regenauer-Lieb, K., and Radlinski, A. P.: Tracking Metamorphic Dehydration Reactions in Real Time with Transmission Small- and Wide-Angle Synchrotron X-ray Scattering: the Case of Gypsum Dehydration, Journal of Petrology, 61, egaa041, https://doi.org/10.1093/petrology/egaa041, 2020.

https://doi.org/10.5194/egusphere-2026-3107
Preprint. Discussion started: 15 June 2026

Schrank, C. E., Gaede, O., Blach, T., et al.: Fast in-situ X-ray scattering reveals stress sensitivity of gypsum dehydration kinetics, Communications Materials, 2, 51, https://doi.org/10.1038/s43246-021-00156-9, 2021.

Schrenk, M. O., Brazelton, W. J., and Lang, S. Q.: Serpentinization, Carbon, and Deep Life, Reviews in Mineralogy and Geochemistry, 75, 575–606, https://doi.org/10.2138/rmg.2013.75.18, 2013.

Selvadurai, A. P. S. and Suvorov, A. P.: Poroelastic properties of rocks with a comparison of theoretical estimates and typical experimental results, Scientific Reports, 12, 10 975, https://doi.org/10.1038/s41598-022-14920-0, 2022.

Shapiro, S. A., Rothert, E., Rath, V., and Rindschwentner, J.: Characterization of fluid transport properties of reservoirs using induced microseismicity, GEOPHYSICS, 67, 212–220, https://doi.org/10.1190/1.1451597, 2002.

Stefan, J.: Über die Theorie der Eisbildung, insbesondere über die Eisbildung im Polarmeere, Annalen der Physik, 278, 269–286, 1891.

Strobl, L. A., Elsworth, D., Fisher, D., and Smye, A. J.: Constraints on the Dehydration Systematics of Subducted Oceanic Crust Across the Blueschist-to-Eclogite Facies Transition (Eclogite Zone, Eastern Alps), Geochemistry, Geophysics, Geosystems, 26, e2025GC012 280, https://doi.org/https://doi.org/10.1029/2025GC012280, e2025GC012280 2025GC012280, 2025.

Sulem, J. and Famin, V.: Thermal decomposition of carbonates in fault zones: Slip-weakening and temperature-limiting effects, Journal of Geophysical Research: Solid Earth, 114, https://doi.org/10.1029/2008JB006004, 2009.

Taetz, S., John, T., Bröcker, M., Spandler, C., and Stracke, A.: Fast intraslab fluid-flow events linked to pulses of high pore fluid pressure at the subducted plate interface, Earth and Planetary Science Letters, 482, 33–43, https://doi.org/10.1016/j.epsl.2017.10.044, 2018.

Turcotte, D. L. and Schubert, G.: Geodynamics, Cambridge University Press, Cambridge, UK, 3rd edn., ISBN 978-1107006539, https://doi.org/10.1017/CBO9780511843877, 2014.

Utkin, I., Khakimova, L., Schmalholz, S. M., and Podladchikov, Y.: Control of nonlinear bulk deformation and large shear strain on first-order phase transformation kinetics, Continuum Mechanics and Thermodynamics, 36, 1195–1214, 2024.

Vitale Brovarone, A., Butch, C. J., Ciappa, A., Cleaves, H. J., Elmaleh, A., Faccenda, M., Feineman, M., Hermann, J., Nestola, F., Cordone, A., and Giovannelli, D.: Let there be water: How hydration/dehydration reactions accompany key Earth and life processes, American Mineralogist, 105, 1152–1160, https://doi.org/10.2138/am-2020-7380, 2020.

Vrijmoed, J. C. and Podladchikov, Y. Y.: Thermolab: A thermodynamics laboratory for nonlinear transport processes in open systems, Geochemistry, Geophysics, Geosystems, 23, e2021GC010 303, 2022.

Wang, H.: Theory of linear poroelasticity with applications to geomechanics and hydrogeology, vol. 2, Princeton university press, 2000.

Watson, E. B. and Wark, D. A.: Diffusion of dissolved SiO_2 in H_2O at 1 GPa, with implications for mass transport in the crust and upper mantle, Contributions to Mineralogy and Petrology, 130, 66–80, https://doi.org/10.1007/s004100050350, 1997.